This is a repository copy of *3D Digital Rock Modeling of the Fractal Properties of Pore Structures*.

3D Digital Rock Modeling of the Fractal Parameters of Pore Structures

Miao Luo[*1], Paul W.J. Glover[2], Peiqiang Zhao[1], Dong Li[1]

1. Hubei Subsurface Multi-scale Imaging Key Lab, Institute of Geophysics and Geomatics,
   China University of Geosciences, Wuhan 430074, China
2. School of Earth and Environment, University of Leeds, Leeds LS2 9JT, UK

*Corresponding author: luomiao@cug.edu.cn

ABSTRACT: Fractal parameters of porous media have been a focus of study in petroleum engineering and hydrogeology for several decades because they provide an effective way to describe the complexity of pore structure across a wide range of scales. This paper combines 3D process-driven digital rock modeling with fractal analysis in order to understand the effect of varying sorting, compaction, cementation, and the fine grain fraction of binary models on the fractal parameters and specific surface area of porous media. Digital rock models (DRMs) were constructed to simulate sandstone using a process-driven modeling technique which simulates sedimentation. The fractal parameters of the resulting pore geometry were calculated using the box-counting method on 2D and 3D representations of the DRMs. Our simulations indicate that increasing compaction or cementation lead to significant decreases in fractal dimension, specific surface area (S_{Sp}) and porosity, showing that these two diagenetic processes can affect the pore microstructure of the rock significantly. While interface fractal dimension (D_i) and S_{Sp} both increase slightly with decreases in sorting (grain size variety), and porosity decreases slightly. Examining the behavior of binary models, the porosity of our digital models shows a V-shaped curve as fine grain fraction increases from 0 to 1, consistent with, but higher than the theoretical values, which we attribute to incomplete packing of the grains arising from the finite boundary of models. The value of both S_{Sp} and D_i increase as the fine grain fraction increases.

KEY WORDS: porous media, 3D digital rock modeling, fractal dimension, specific surface area, porosity

0   INTRODUCTION

The pore microstructures of porous media such as sandstones, limestones, shales and soils are important in the study of petrophysics, subsurface geophysics, and reservoir engineering, since most of the world's underground water, oil, gas and gas hydrate reserves are stored in them. Furthermore, porous rocks are increasingly also being used for the long-term storage of CO_2 and the shorter term storage of hydrocarbon gases and energy in the form of compressed air.

It is well known that the geometry of pore space is highly tortuous, disordered and complex over a wide range of scales (Krohn, 1988a; 1988b). This complexity has great effects on the electrical conductivity (Katz and Thompson, 1985; Suman and Knight, 1997; Revil and Glover, 1998; Zhao et al., 2013; Luo and Pan, 2015), permeability (Hansen and Skeltorp, 1988; Schlueter et al., 1997; Pape et al., 1999; Yu and Cheng, 2001; Wu; et al., 2019), imbibition (Cai and Yu, 2011), and other properties of porous media. Despite this however, it is difficult to evaluate the complexity of pore spaces and its impact on the other petrophysical properties quantitatively.

Most natural porous media are composed of solid grains of various shapes and dimensions. Their pore structure presents an approximately self-similar geometry (Mandelbrot, 1982; Katz and Thompson, 1985; Hansen and Skjeltorp, 1988; Xie, 1993). In recent decades, fractal theory has been used increasingly in the study of surface roughness (Wong, 1986; Xie, 1993: Glover et al., 1994), pore structure analysis (Muller, 1996; Dutta and Tarafdar, 2003; Giri, 2012; Giri et al., 2013), fractal fracturing (Isakov et al., 2001; Ogilvie et al., 2003; 2006), heterogeneity (Karimpouli and Tahmasebi, 2018) and permeability evaluation (Hansen and Skeltorp, 1988; Pape et al., 1999; Al-Zainaldin et al., 2017; Glover et al., 2018). Numerous studies have indicated that fractal dimension is an ideal parameter to describe the complexity of pore structure (Katz and Thompson, 1985; Krohn, 1988a; Krohn, 1988b; Muller, 1996; Dutta and Tarafdar, 2003; Giri, 2012; Giri et al., 2013; Wu; et al., 2019), but there is little information showing the effect of depositional process on the fractal dimension of a granular porous medium.

In order to obtain the fractal dimension of an object, researchers developed several different computing methods which are now standard mathematical tools. These tools include the box-counting method (Russell et al., 1980), the fractional Brownian motion method (Mandelbrot, 1975), and the area measurement method (Shelberg et al., 1983; Peleg et al., 1984). However, the box-counting method is the most frequently used algorithm for computing the fractal dimension of images, and is implemented in this work.

The box-counting method is widely used to calculate the fractal dimension of complex patterns, because it is easy to apply and applicable for patterns both with and without deterministic self-similarity (Peitgen et al., 1992). In the box-counting algorithm, the resolution of images, the pre-processing of images and selection of the range of box size

could all affect the computation of fractal dimensions. Consequently, significant efforts have been made to improve the accuracy of the estimation of fractal dimensions (Sarkar and Chaudhuri, 1992; Jin et al., 1995; Baveye et al., 1998; Buczkowski et al., 1998; Gonzato et al., 1998; Foroutan-pour et al., 1999; Bisoi and Mishra, 2001; Xu and Weng, 2006; Pruess, 2007; Li et al., 2009).

Digital rock modeling (DRM) techniques have developed rapidly in recent years. There are mainly two ways to construct rock models. One way is based on physical measurements (e.g. X-ray CT, SEM, FIB-SEM) of rock samples; the other way is based on computer simulation. Most of the physical measurements can provide real 2D and 3D image of rocks, but they are usually very expensive and time-consuming. While the computer simulation provides a convenient, inexpensive, efficient and flexible way to build rock models and generate pore scale images. The most popular DRM techniques by computer simulation include the process-driven method (Bakke and Øren, 1997; Coelho et al., 1997; Jin et al., 2003; Nilsen et al., 1996; Øren et al., 2002; Pilotti, 2000; Zhu et al., 2012), the multiple point statistic method (Okabe and Blunt, 2005; Tahmasebi and Muhammad Sahimi, 2012), the continuum geometrical method (Biswal et al., 2007, 2009; Latief et al., 2010; Roth et al., 2011), the bidisperse ballistic deposition modelling (Tarafdar and Roy, 1998; Dutta and Tarafdar, 2003), and the stochastic method (Hazlett, 1997; Yeong and Torquato, 1998; Eschricht et al., 2005; Wu et al., 2020a; Wu et al., 2020b). These techniques provide us an ideal way to simulate a wide range of different rock textures with complex pore structures.

In our study, the process-driven digital rock modeling approach is employed to build the 3D models using monodisperse and polydisperse spherical grains. The digital rock modeling process generates pore-scale images of porous media in three dimensions which can be analysed either in three dimensions or by using two-dimensional intersections through the 3D data volume. The box-counting method was then used to analyze the images and compute the fractal dimensions of pore structure. With the advantages of the process-driven DRM approach, we can control the size of all the grains comprising the models, and evaluate the effects of grain sorting, compaction and cementation on the fractal dimensions, porosity, and specific surface area of porous media.

1 METHODOLOGY

The two important methods involved in this study are (i) process-driven digital rock modeling, which is used to construct the sandstone models, and (ii) the box-counting method for computing the fractal dimensions of pore structure.

1.1 Model construction

The advantage of the process-driven approach to DRMs creation is that it creates realistic pore structures which represent sedimentary rocks well because the process of sedimentation is mirrored in the process by which the DRMs are constructed. Consequently, process-drive DRMs

represent primary depositional textures well, and the structure can then be modified to account for compaction and diagenesis. The method usually treats the three processes as three distinct steps; (i) sedimentation, (ii) compaction, and (iii) diagenesis (Bakke and Øren, 1997). In this study, our simulations implement only very simple rock models, consisting of a single mineral component represented by grains of various sizes. The pore structure is that space which is not occupied by grains. While much more complex models are easily possible, increasing complexity, by making models multi-mineralic for example, makes the results more difficult to interpret physically. Consequently, this work starts with the simplest scenarios and restricts itself to spherical grains.

We have developed code to construct 2D and 3D sandstone models. The code is implemented in Matlab and uses the native program libraries. Studies based on the 2D models have been reported in one of our previous papers (Li et al., 2019). However, it was recognized that significant systematic errors could arise from restricting the modelling to two dimensions. In this work, we extend the creation and testing of DRMs to three dimensions. However, we will describe the process-driven approach using figures in two dimensions for clarity in print. Figure 1a-d shows schematically the sedimentation of spherical grains with a certain distribution of radii. Figure 1a shows a new (red) grain that has been generated randomly in order to conform to a pre-programmed grain size distribution, and is falling. Figure 1b shows the previous deposited grains are expanded according to the radius of the new grain and form a deposit surface where the centre of the new grain can be placed at. Figure 1c shows that the new grain finds a stable position, which globally minimizes its gravitational potential energy. Figure 1d shows the image of a digital rock which is formed by the sedimentation of a cohort of such grains. It is worthwhile noting that the pore space beneath the red grain, once it has settled, was capable of being occupied by a smaller grain. However, at the time of deposition, a smaller grain was not available. We call this effect incomplete packing. It occurs naturally, and shows how the sedimentation-driven DRM can incorporate this effect in a realistic way.

Once the primary depositional structure has been created, we can subject it to compaction and cementation effects to obtain a more realistic rock model.

Compaction can be implemented in two ways. In the first, the volume of the entire model is reduced by allowing the grains to overlap. The overlapping material is then removed. This process models the loss of matrix material by diagenetic dissolution. Moreover, the greatest loss of material occurs where the grains touch, which means that this process may model the process of pressure solution well. If the rock represents an open flow system such that the dissolved material is removed completely from the rock, this process results in a reduction of porosity because the loss of the bulk volume is always greater than the loss of overlapping material. If the flow system is closed, precipitation may occur, which will decrease the porosity of the rock further.

In the second implementation of compaction, the overlapping material is not removed, but broken off and redistributed in the pores. This process models purely mechanical compaction by grain comminution. Purely mechanical compaction leads to a greater loss of porosity than that encountered for dissolution in an open system, as described immediately above, but may be

similar to that encountered if dissolved material is redeposited locally by precipitation in a closed flow system. We implement compaction assuming the material to be removed, which gives an overall small reduction in porosity (Fig. 1f).

Cementation can also be added to the model (Fig. 1g). In our case we implement it by adding a uniform layer around grains where there is space to do so (i.e., not where grains touch). This approach to cementation is similar to that observed in nature, and results in an overall reduction in porosity.

The final DRMs can be subject to edge effects, which arise from their creation. To reduce the edge effect of the box model, we carried out all of our analyses on sub-volumes of the entire model, which are sufficiently far from the periphery of the DRMs to obviate most edge-related artefacts. Figure 2 shows a flowchart describing the detailed procedure of the process-driven digital rock model construction.

1.2   Fractal dimension and specific surface area calculation

Fractal (self-similar) structures are very common in nature. Examples include coastlines, mountains, clouds (Mandelbrot, 1982), river networks (Tarboton et al., 1998), natural fracture sizes (Ogilvie et al., 2001), fracture surfaces (Glover and Hayashi, 1997) and fluid flow within natural fractures (Glover et al., 1997; 1998a; 1998b; Ogilvie et al., 2006), and the pore structure of sandstones (Krohn, 1988; Schroeder, 1991; Li et al., 2009). Thirty years ago it was recognized that the geometrical characteristics of these objects (e.g., length, area and roughness) are too complex to be described accurately by traditional Euclidean geometry. Therefore, a fractal dimension, which is a non-integer dimension, was defined and proposed to describe the fractal features of complex objects quantitatively (Mandelbrot, 1982).

The fundamental definition of fractal dimension calculation is based on the theory of self-similarity. Self-similarity occurs when for a bounded set A in Euclidean space, A is the union of N_r distinct copies of itself, where each is similar to A scaled down by a ratio r. Thus, the fractal dimension D of the bounded set A can be expressed as

$$D = \lim_{r \to 0} \frac{\log(N_r)}{\log(1/r)}, \tag{1}$$

where N_r is the least number of distinct copies of A at the scale r (Mandelbrot, 1982; Bisoi and Mishra, 2001; Li et al., 2009; Wang et al., 2012).

Equation (1) can be used directly for those objects with ideal and deterministic fractals. For the objects without deterministic fractals, researchers have developed other methods to estimate their fractal dimensions, such as the box-counting method (Russell et al., 1980), the power spectrum method (Turner, 1998), and the perimeter-area relationship method (Mandelbrot, 1982).

There are a large number of measurements that may be made on a porous medium, many

of which may be fractal. Putting those associated with fractures aside for simplicity, an inexhaustive list may include grain and pore volume, grain size, grain surface area and the area of the pore/grain interface (Krohn, 1988b; Schroeder, 1991; Li et al., 2009). We have chosen to study mainly the pore volume and surface area of the pore/grain interface in a 3D rock as these properties are important for applications involving rock-fluid interaction such as processes associated with surface conduction (Glover, 2015; Glover et al., 1994), sorption of pollutants, and sorption of radioisotopes in repositories for nuclear waste (Ghanbarian-Alavijeh et al., 2011; Brouers and Al-Musawi, 2018; Wang et al., 2019) as well as the transport and attenuation of elastic waves and heat through porous media (Yu et al., 2018; Gudehus and Touplikiotis, 2016).

We have developed a Matlab code to compute the fractal dimension of 2D and 3D images of digital rocks based on the box-counting method reported previously (Foroutan-pour et al., 1999). Taking a 2D image as a simplified example, the computation process can be summarized in the following steps:

1. Take a 512×512 pixels sized square sub-area of the digital rock model (Fig. 3a and 3b).

2. The analysis may now be carried out for the distribution of pore volume or the pore/grain boundary. The former is described by the upper panels in Fig. 3 (i.e., Fig. 3c1 to 3e1), while the pore/grain boundary is described by the lower panels in Fig. 3 (Fig. 3c2 to 3e2). In order to obtain the fractal dimension of the pore/grain boundary, the interfaces between the pores and the solid particles are obtained by digital filtering, and are shown in Fig. 3c2 and 3d2 as white lines, making all the other parts of the sample black (i.e., the pore and grain parts). In order to obtain the fractal dimension of the pores, no further filtering is required.

3. The image is gridded with a mesh of density $n_i \times n_i$ (where $n = 2^i$, i is an integer), thus the side length of each box is $r_n = 512/n$. All the boxes which contain white pixels are summed to obtain a count number N_r, (Fig. 3c1). In our case, the mesh density usually ranges from 2×2 up to 256×256.

4. The mesh density is then increased to $n_{i+1} \times n_{i+1}$ (where $n_{i+1} = 2^{i+1}$). Now the side length of each box is $r_n = 512/n_{i+1}$. Once again all the boxes which contain the white pixels are summed to obtain a new count number N_r, (Fig. 3d1).

5. Step 4 is repeated, incrementing i by one until $i=8$ (i.e., a minimum box size of 2×2 pixels. Hence, we can obtain multiple pairs of (r_n, N_r) data.

6. A least-squares regression of $\log(N_r)$ as a function of $\log(1/r)$ can then be performed on the (r_n, N_r) dataset, and the fractal dimension is obtained from the slope of the fitted line (Fig. 3e1 and 3e2). Hence, the fractal dimension of both the pore area D_a (Fig. 3e1) and the pore boundary D_b can be obtained (Fig. 3e2).

The same procedures can be modified to analyse the analogue properties of three dimensional DRMs. Hence, we can compute the fractal dimension of the pore volume D_v and that of the pore/grain interface D_i by using 3D images of porous rock.

In this work the specific surface area (S_{Sp}) is defined as the ratio of the total surface area of pore space to the total volume of pore space.

2   RESULTS

In order to reveal the potential influencing factors of the fractal dimension of porous media, we have calculated the fractal dimension parameters, porosity and specific surface area while varying the sorting, compaction, cementation and the fine grain fraction of binary models, one at a time.

2.1   The effect of sorting (grain-size variety)

Grain size variety is a good indicator of the sorting of grains. We have constructed seven types of model with varying grain-sizes.

Table 1 lists the 7 grain-size mixtures examined in this paper, together with the modelling results for porosity, specific surface area and four types of fractal dimension. In each case the maximum grain size is 26 units. Mixture V1 is single-sized. Mixture V2 is bimodal with grains of 26 units together with others of 23 units. Subsequent mixtures add one more grain size to the mixture, always 3 units smaller each time. The process-driven depositional code was programmed to choose at random between available grain sizes with equal chances amongst the types available. Consequently, the result of modelling with the V2 mixture is a final model composed by number of 50% of grains of radius 26 units and 50% of grains of radius 23 units (but 59.1% to 40.1% on the basis of volume). By contrast Model V7 contains equal numbers of grains of 7 different sizes (14.28% or each), with the large grains contributing significantly more to the fractional volume (37.2%) than the smallest grains (1.08%).

Figure 4 shows images of 3D models with different grain size variety. It is clear that, at least qualitatively, Model V1, which contains grains of one size, shows larger pore size, while Model V7, which contains grains of seven sizes, has smaller pore sizes.

Figure 5 shows the evolution of the fractal dimension, specific surface area and porosity as grain size variety increases. Figure 5a and 5b shows that the fractal dimensions D_i and D_b increase slightly with increasing grain-size variety, while there is no significant change in D_v and D_a. Figure 5c shows that the specific surface area (S_{Sp}) increases slightly with the increase of grain size variety, which is consistent with the grain surface area to grain volume ratio (SA/V = $3/r$) decreasing in inverse proportion to grain size r. Figure 5d shows that the porosity decreases slightly as the grain size variety increases, which indicates the propensity for small grains to fill gaps created between the larger grains. The extent to which this was the

case in our modelling reflects the relatively small volume fractions of the smallest grains in the mixtures. Repeating the experiments with grain availability being uniform on the basis of grain volume is expected to produce significantly larger variabilities for S_{Sp} and porosity, but is not included in this paper, and would be recommended further step in modelling.

2.2 The effect of compaction

We have also attempted to investigate the evolution of fractal dimension, specific surface area and porosity with simplified compaction using our digital rock models. Figure 1 (parts d and e) shows schematic diagrams of the way we have implemented compaction. We constructed an initial digital rock model composed of grains with radius of 24, 20, 16 and 12 units before imposing different degrees of compaction on it. We quantify the degree of compaction using a compaction coefficient, C_p and the compaction effect can be expressed by

$$x = x_o(1-C_{p1}), \tag{2}$$
$$y = y_o(1-C_{p2}), \tag{3}$$
$$z = z_o(1-C_{p3}), \tag{4}$$

where x, y, and z are the position coordinates of the centre of a grain after the compaction, x_o, y_o, and z_o are the initial position coordinates of the centre of the grain, and C_{p1}, C_{p2}, and C_{p3}, are the compaction coefficient ($1 > C_p > 0$) along x-axis, y-axis and z-axis, which is proportional to the compaction effect. If the C_p tends to 0 there is no compaction, and if C_p tends to unity the compaction is so severe that only a single layer of grains remains. In this work we have used a range $0.24 > C_p > 0$ and $C_{p1} = C_{p2} = C_{p3} = C_p$.

Table 2 shows the modeling data of the porosity, specific surface area and four types of fractal dimension for the models with different compaction coefficients C_p. Figure 6 shows some 3D models with different compaction coefficients. Comparing them, it is clear that porosity decreases significantly with the increase of compaction coefficient but it is difficult to form a qualitative assessment of how the fractal dimension and specific surface area might change.

Figure 6a shows the initial state of the model without compaction. The model is then compacted by squeezing and overlapping the grains in the vertical and horizontal directions. This is formally the same as considering all the material from one of the grains in the overlap being removed from the model by a process such as dissolution and transport out of the model. Consequently, the implementation of compaction in this work reflects both the vertical and horizontal stress and pressure dissolution occurring to remove material (Renard and Dysthe, 2003).

Figure 7 shows that the porosity and fractal dimension parameters decrease as compaction increases, while specific surface area significantly increases while the compaction coefficient increases. It is clear that the process of compaction is, to some extent, simplifying

the complexity of the pore structure at the same time as the porosity is being significantly reduced.

2.3 The effect of cementation

The third model factor we have investigated is cementation. To do this we constructed an initial digital rock model composed of grains with radius of 26, 23, 20 and 17 units. We then induced different degrees of cementation to the model. It was assumed that the cementation took the form of a uniform layer of cement which grew on the surface of the original grains as shown in Figure 1f. This has the effect of enlarging the grains, but only at the points where the original grains are not touching. The degree of cementation has been quantified by using a cementation thickness. The cementation effect then is given by the following equation:

$$R = R_o + T_c \tag{5}$$

where R_o is the radius of a grain without cementation, R is the radius of the grain after cementation, and T_c is the thickness of cement layer. The implementation of the digital rock models is such that we can make the grains larger, representing cementation, and automatically discount the material which overlaps neighboring grains. In this way it is possible to generate the required geometries with very simple changes to our code.

Table 3 shows the computing data of the porosity, specific surface area and four types of fractal dimension of the models with different cementation thickness.

Figure 8 shows some 3D models with different cementation thickness. Fig. 8(a) shows a model with no cementation ($T_c = 0$), while Fig. 8(c) shows a model with significant cementation effect ($T_c = 8$). Once again, these qualitative diagrams show clearly that the porosity decreases significantly. Furthermore, as cementation thickness increases the pore spaces become increasingly boxy in nature. It is expected that this geometry will have a lower fractal dimension. This hypothesis is borne out in Figure 9, which shows how the fractal dimension and porosity varies as the cementation thickness increases. However, the specific surface area increases significantly as the cementation thickness increases. This may be attributed to the poor connectivity of pores when the cementation thickness is large.

2.4 The effect of the fine grain fraction of binary models

We have also investigated so-called binary models, i.e., models composed of two types of grains (coarse and fine) in order to test a recently published theory of binary mixing (Glover and Luo, 2020). When the ratio of the diameters of coarse and fine grains is large enough, it is clear that porosity depends upon the extent to which smaller grains can pack between larger grains. However, mathematically, this also occurs to a limited extent when the relative rations of coarse and fine grains is closer providing there is imperfect packing.

Figure 10a shows a schematic diagram of 2D binary mixtures of spherical grains where

the volume fraction of fine grains increases from zero to unity from the left to the right of the diagram (modified from Glover and Luo, 2020). The figure shows two competing processes, which were called the Interstitiation Process (IP), and the Replacement Process (RP) by Glover and Luo (2020). The IP process operates at low volume fractions of fine grains, where smaller grains fill the interstices between larger grains (reading from the left of Figure 10a, in the direction from the left to the right). The RP process operates at high volume fractions of fine grains, where coarse grains replace groups of fine grains as well as the pore space between them (reading from the right of Figure 10a, from the right to the left).

The porosity of the binary mixture arising from such processes is a function of the volume fraction of the fine grains (Zhang et al., 2009; Glover and Luo, 2020), and their relation can be described by the following equations,

$$
\left.\begin{array}{l}
\phi_n = \dfrac{\phi_c - \chi_{Vf}}{1 - \chi_{Vf}} \quad \text{for } \phi_n \geq \phi_{\min} \quad \text{and} \quad \chi_{Vf} \leq \chi_{Vfcrit} \\[3mm]
\phi_N = \phi_f \left[\dfrac{\chi_{Vf}}{\left(1 - \phi_f + \phi_f \chi_{Vf}\right)} \right] \quad \text{for } \phi_n \geq \phi_{\min} \quad \text{and} \quad \chi_{Vf} \geq \chi_{Vfcrit} \\[3mm]
\phi_{\min} = \phi_c \phi_f = \dfrac{\phi_c - \chi_{Vfcrit}}{1 - \chi_{Vfcrit}} \quad \text{and} \quad \chi_{Vfcrit} = \dfrac{\phi_c - \phi_{\min}}{1 - \phi_{\min}}
\end{array}\right\}, \qquad (6)
$$

where ϕ_n represents the theoretical porosity of the Interstitiation Process and decreases as the fraction of the fine grains (χ_{Vf}) increases; ϕ_N represents the theoretical porosity of the Replacement Process and increases as the fraction of the fine grains (χ_{Vf}) increases; ϕ_{min} represents the theoretical minimum porosity of a binary mixture; ϕ_c is the porosity of pure coarse grains; ϕ_f is the porosity of pure fine grains; χ_{Vfcrit} is the fractional value of the fine grains where the porosity decreases to the minimum.

The theoretical approach predicts that the porosity decreases at first and then increases as the fine grain fraction increases (Figure 10b), with the minimum porosity occurring for some mixture of fine and coarse grains. The Glover and Luo (2020) model represents a lower limit for the porosity not taking into account imperfect packing. Imperfect packing leads to porosities above the theoretical curves if the two end-members (ϕ_f and ϕ_c) exhibit better packing. The process-driven digital rock modeling approach we use usually can only produce imperfect packing models.

We have constructed 3D binary models using our process-driven digital rock modeling approach. We can compare our digital results with the theoretical calculations. Figure 11a

indicates that the porosity of our digital models also shows a V-shape curve and is higher than the theoretical porosity, which means our digital binary models did not reach a complete packing and produced relatively high porosity. The Interstitiation Process (IP) describes the low F_s porosity behavior well, while the Replacement Process (RP) does not describe the high F_s behavior, since the data from the digital rock models can only be fitted by the IP curve at the left part of Figure 11a.

The model with higher size ratio of coarse and fine grains displays lower porosity (Figure 11a), so the grain size ratio can also affect the porosity of the binary model. Figure 11b, 11c and 11d indicate that the specific surface area and two fractal dimension parameters increase as the fine grain fraction increases.

3   DISCUSSION

3.1   Grain size variety and fine grain fraction

Both the fine grain fraction of binary models and grain-size variety are related to the sorting of grains and affect the initial deposition state of the sedimentary rocks. The 3D digital rock modelling carried out in this paper provides us with a quick look at the effect of fine grain fraction and grain-size variety on the fractal dimension, specific surface area and porosity of porous media. These variables are also associated with the initial deposition of the rock, and hence associated with the rock's initial microstructure and primary porosity.

Our digital rock modelling shows that fractal dimension parameters D_i and D_b and specific surface area increase slightly with increasing grain-size variety, within the parameter range studied in this work (Fig. 5), while the porosity decreases slightly. In other words, the availability of a range of grain sizes allows a more efficient packing, reducing the porosity, while the resulting packing is more complex.

This effect was also apparent in the binary modelling. Here, the radius ratio of the coarse to fine grains in the binary model affected the primary porosity throughout the entire mixing range (from 100% coarse grains to 100% fine grains) and the minimum porosity (Fig. 11a), which occurs between 0.17 and 0.25. The porosity was found to increase with decreasing coarse to fine grain size ratio. This is consistent with the expected behavior, which, for a binary mixture, allows small grains to better access and occupy spaces formed between larger grains if the coarse to fine grain size ratio is large. For smaller values of this ratio, the two grain sizes are nearer each other, and hence small spaces between the larger grains cannot be as easily occupied by the smaller of the two grain sizes.

Theoretically, we should have $\phi_c = \phi_f$ in Fig. 11a, since porosity is scale independent. Actually, the experiment data by Glover and Luo (2020) and our numerical simulations do not support this phenomenon. The main reason is the boundary effect of the vessel (model). Due to the size limitation of the vessel (model), vessel boundary can affect the arrangement of all the grains. This hinders the model from getting to the closest packing. The other reason is the

image resolution when we use digital rock models. For a given resolution, the surface of a large sphere is always much smoother than that of a small one.

By contrast, the specific surface area and fractal dimensions were found to exhibit a different behavior, which has not been predicted by previously existing models (Yang, et al., 2014; Gao, et al., 2017). Specific surface area S_{Sp} increases as the fraction of fine grains in the mix is increased with no critical mixing fraction at which S_{Sp} has a minimum value (Fig. 11b). Once again, this is expected. The surface area to volume ratio for spheres (and many other solids) increases as the size of the grain is reduced. The observed DRMs modelled results are simply the operation of this basic geometrical relationship in a model of fixed volume. The increase of S_{Sp} with increasing fraction of fine grains is more marked for mixtures with large coarse to fine grain size ratios, which is due to the larger surface area to volume ratios exhibited by smaller grains as well as the efficiency with which the addition of fine grains between the larger grains in the matrix add to the overall surface area. This process occurs up until a fraction of small grains which is about the same as the critical fraction shown in the porosity diagram (Figure 11a). After this point has been reached the addition of smaller grains must be carried out by the removal of the larger grains, hence the process of increasing the surface area is less efficient, because it must be the result of the net effect of removal of the surface area of the larger grains and addition of the surface area of the smaller grains to replace the larger grain.

Interestingly, the interface fractal dimension D_i also shows a very similar behavior to S_{Sp} (comparing Fig. 11b to Fig. 11c), while the volume fractal dimension D_v shows a similar behavior to the porosity (comparing Figure 11a to Figure 11d). These associations suggest that the pairing S_{Sp} and D_i , and the pairing ϕ and D_v both depend on the same geometrical constraints.

We have carried out a set of cross plots to examine interdependence between these four parameters, as shown in Figure 12. As expected, the relationship between specific surface area and D_i is fairly linear, with very similar behavior for all three binary models taking part in the Interstitiation Process, trifurcating when the Replacement Process takes over at larger fractions of finer grains. The other cross plots show more complex behavior, but generally all three binary models have the same behavior during interstitiation, that follow different but often parallel curves during replacement.

The behavior of the volume fractal dimension D_v is more complex and worth examining explicitly. The results of D_v as a function of the fraction of fine grains (Figure 11d) shows an initial decrease to a minimum value of D_v, followed by an increase in D_v. This is similar behavior to that exhibited by the porosity, but is different in two important ways. First, the critical value of the fraction of fine grains at which the minimum value of D_v occurs is not the same as that for porosity, but occurs at about half the value of the fraction of fine grains (between 0.1 and 0.2). Second, binary mixtures with a large coarse to fine grain size ratio exhibit a greater increase in D_v with increasing grain size ratio, which is the opposite of what

is observed for porosity. This suggests, counterintuitively, that greater complexity of pore space is associated with binary mixtures of two grain sizes which are similar. The cross-plot of porosity against D_v (Fig. 12d) shows that there is some relationship between these two parameters, but it is complex, with the critical value (lowest value of the parameter) for porosity and D_v being different, which contrasts with the situation when one compares porosity with D_i (Fig. 12c), where they are much more consistent between each of the new models.

3.2 Compaction and cementation

The situation is rather different in the case of the diagenetic processes that modify the initial rock microstructure. Here, the fractal dimension and porosity decrease rapidly with increasing compaction and cementation effect (Fig. 7 and Fig. 9). While the loss of porosity is to be expected, one would imagine that both compaction and cementation would leave the rock pore space with a more complex microstructure and with a correspondingly higher fractal dimension. That this is not so in the results presented in this work may be associated with the simplifying assumption in this research of using only round grains. It may be the case that more sophisticated models are needed; models which take into account other important influencing factors such as grain shape, grain size distribution, rupture, deformation etc. These models are in the process of being designed.

However, both the compaction and cementation processes implemented in this work do not reduce pore volume randomly, but operate at grain boundaries, like their natural analogues. This form of pore volume reduction preferentially removes porosity that is not in the centre of pore volumes or the flow channels that they may form. Consequently, it is possible that the reduction in both D_i and D_v reflect a decrease in complexity of the pore space as more direct channels are formed by blocking side cul-de-sac. If this interpretation is correct we would expect there to be a minimum in both D_i and D_v followed by increasing fractal dimensions as C_p and T_c are increased past the point where compaction and cementation is blocking entire pathways for flow, i.e., close to the percolation threshold.

3.3 Relationships between porosity, specific surface area and fractal dimension

The relationships between the fractal dimension and their associated porosities and specific surface areas can be analysed using the results of numerical simulations on our DRMs. Besides the DRMs, we computed the fractal dimension of 12 real sedimentary rocks by their micro-CT images that published by Dong and Blunt (2009) (Table 4).

Figure 13a and 13b show that the fractal dimension parameters D_v and D_i have positive correlations with porosity. Figure 13c shows that the specific surface area (S_{Sp}) has a negative correlation with porosity. Figure 13d shows that the specific surface area (S_{Sp}) has a negative correlation with the fractal dimension parameter D_v for the data from the cementation and compaction modelling.

The cementation and compaction effect produce very similar impact on the porosity, specific surface area and fractal dimension (Fig. 13). The data from the grain size variety modelling show a very narrow span in the parameter space (Fig. 13). Therefore, the effect of grain size variety on porosity, fractal dimension and specific surface area is relatively weak.

The data from the real rocks show a relatively narrow span in the parameter space too (Fig. 13). This indicates the real rocks did not experience very fierce cementation and compaction effects. Moreover, most of the data points from the real rocks fall into the span space of the digital rocks' data.

The results above indicate that the model parameters (e.g. cementation and compaction) of digital rock models can be adjusted easily and the simulated data can cover a larger range in the parameter space than the real rocks' data. This is an important advantage of DRMs.

4 Conclusions

Using the process-driven digital rock modeling technique, we can easily construct digital rock models to simulate porous media (e.g., sandstones) and control the size of all the grains of which the models are composed. Our work demonstrates the advantage of digital rock modeling in the research of pore structure and its fractal features.

The multiple model implementations carried out in this work indicate that:

(1) the diagenetic processes of compaction and cementation give rise to significantly smaller fractal dimensions, specific surface area and porosities, as expected. This implies the development of less complex pore microstructures.

(2) grain size variety (sorting) produces a much weaker impact on porosity, fractal dimension and specific surface area than compaction and cementation. Fractal dimension parameters D_v and D_a display even no correlation with grain size variety.

(3) for the binary models, the porosity of our digital models shows a V-shape curve as fraction of fine grains increases from 0 to 1, but our porosity is higher than the theoretical porosity due to the incomplete packing of the binary grains. The specific surface area and fractal dimension D_i and D_v increase as the fine grain fraction increases.

(4) the computation of the micro-CT image data of sedimentary rocks released by Dong and Blunt (2009) shows that that fractal dimension parameters D_i and D_v and specific surface area do not show obvious correlations with permeability, but succolarity (σ) shows a positive linear relationship with permeability (coefficient of determination $R^2 = 0.85$). Therefore, the succolarity of the rocks may give a better correlation to permeability than porosity ($R^2 = 0.721$).

(5) the best relationship to permeability was found to be the product of porosity and succolarity to the power of n and a coefficient S, where n is approximately 3 and S is a coefficient that we hypothesize depends on pore or pore throat size.

ACKNOWLEDGEMENTS

REFERENCES CITED

Al-Zainaldin, S., Glover, P.W.J., Lorinczi, P., 2017. Synthetic fractal modelling of heterogeneous and anisotropic reservoirs for use in simulation studies: Implications on their hydrocarbon recovery prediction. *Transport in Porous Media*, 116(1): 181–212.

Bakke, S., Øren, P., 1997. 3-D Pore-scale modelling of sandstones and flow simulations in the pore networks. *SPE*, 35479.

Baveye, P., Boast, C.W., Ogawa, S., et al., 1998. Influence of image resolution and thresholding on the apparent mass fractal characteristics of preferential flow patterns in field soils. *Water Resources Research,* 34 (11): 2783–2796.

Bisoi, A.K., Mishra, J., 2001. On calculation of fractal dimension of images. *Pattern Recognition Letters,* 22: 631–637.

Biswal, B., Øren, P.E., Held, R.J., et al., 2007. Stochastic multiscale model for carbonate rocks. *Physical Review E,* 75: 061303.

Brouers, F., Al-Musawi, T.J., 2018. Brouers-Sotolongo fractal kinetics versus fractional derivative kinetics: A new strategy to analyze the pollutants sorption kinetics in porous materials. Journal of Hazardous Materials, 350: 162-168

Buczkowski, S., Kyriacos, S., Nekka, F., et al., 1998. The modified box-counting method analysis of some characteristic parameters. *Pattern Recognition,* 31(4): 411–418.

Cai, J., Yu, B., 2011. A discussion of the effect of tortuosity on the capillary imbibition in porous media. *Transport in Porous Media,* 89(2): 251–263.

Coelho, D., Thovert, J.F., Adler, P.M., 1997. Geometrical and transport properties of random packings of spheres and aspherical particles. *Physical Review E,* 55: 1959–1978.

Coker, D.A., Torquato, S., Dunsmuir, J.H., 1996. Morphology and physical properties of Fontainebleau sandstone via a tomographic analysis. *Journal of Geophysical Research*: *Solid Earth*, 101:17497-506.

Dong, H., Blunt, M.J., 2009. Pore-network extraction from micro-computerized-tomography images. *Physical Review E*, 80 (3), 036307.

Dutta, T., Tarafdar, S., 2003. Fractal pore structure of sedimentary rocks: simulation by ballistic deposition. *Journal of Geophysical Research,* 108 (B2): 2062-2067.

Eschricht, N., Hoinkis, E.,Mädler, F., et al., B., 2005. Knowledge based reconstruction of random porous media. *Journal of Colloid and Interface Science*, 291: 201-213.

Flannery, B.P., Deckman, H.W., Roberge, W.G., D'Amico, K.L., 1987. Three-dimensional X-ray

microtomography. *Science*, 237: 1439-44

Foroutan-pour, K., Dutilleul, P., Smith, D.L., 1999. Advances in the implementation of the box-counting method of fractal dimension estimation. *Applied Mathematics and Computation,* 105: 195–210.

Gao, D., Li, M., Wang, B., Hu, B., Liu, J., 2017. Characteristics of pore structure and fractal dimension of isometamorphic anthracite. *Energies*, 10(11): 1881

Ghanbarian-Alavijeh, B., Millan, H., Huang, G., 2011. A review of fractal, prefractal and pore-solid-fractal models for parameterizing the soil water retention curve. *Canadian Journal of Soil Science*, 91(1):1-14

Giri, A., Tarafdar, S., Gouze P., et al., 2012. Fractal pore structure of sedimentary rocks: simulation in 2-d using a relaxed bidisperse ballistic deposition model. *Journal of Applied Geophysics,* 87: 40–45

Giri, A., Tarafdar, S., Gouze, P., et al., 2013. Fractal geometry of sedimentary rocks: Simulation in 3-D using a Relaxed Bidisperse Ballistic Deposition Model. *Geophysical Journal International*, 192: 1059–1069.

Glover, P.W.J., Meredith P., Sammonds P., et al., 1994. Ionic surface electrical conductivity in sandstone. *Journal of Geophysical Research*, 99(B11): 21635–21650.

Glover, P.W.J., Matsuki, K., Hikima, R., et al., 1997. Fluid flow in fractally rough synthetic fractures. *Geophysical Research Letter*, 24(14): 1803–1806.

Glover, P.W.J., Hayashi, K., 1997. Modelling fluid flow in rough fractures: Application to the Hachimantai geothermal HDR test site. *Physics and Chemistry of the Earth,* 22(1-2 SPEC. ISS.): 5–11.

Glover, P.W.J., Matsuki, K., Hikima, R., et al., 1998a. Fluid flow in synthetic rough fractures and application to the Hachimantai geothermal hot dry rock test site. *Journal of Geophysical Research*, 103(5): 9621–9635.

Glover, P.W.J., Matsuki, K., Hikima, R., et al., 1998b. Synthetic rough fractures in rocks. *Journal of Geophysical Research,* 103(5): 9609–9620.

Glover, P.W.J., 2015. Geophysical Properties of the Near Surface Earth: Electrical Properties. Treatise on Geophysics: Second Edition. pp. 89-137.

Glover, P.W.J., Lorinczi, P., Al-Zainaldin, et al., 2018. Advanced fractal modelling of heterogeneous and anisotropic reservoirs, SPWLA 59th Annual Logging Symposium 2018.

Glover, P.W.J., Luo, M, 2020. The porosity and permeability of binary grain mixtures. *Transport in Porous Media*, 132(1), 1–37.

Gonzato, G., Mulargia, F., Marzocchi, W., 1998. Practical application of fractal analysis: problems and solutions. *Geophysical Journal International,* 132: 275–282.

Gudehus, G., Touplikiotis, A., 2016. Wave propagation with energy diffusion in a fractal solid and its fractional image. *Soil Dynamics and Earthquake Engineering*, 89:38-48

Han, S., Cheng, Y., Gao, Q., et al., 2019. Investigation on heat extraction characteristics in randomly fractured geothermal reservoirs considering thermo‐poroelastic effects. *Energy Science &*

Engineering, 2019, 7(5): 1705-1726

Hansen, J. P., Skeltorp, A. T., 1988. Fractal pore space and rock permeability implications. *Physical Review B,* 38: 2635–2638.

Hazlett, R.D., 1997. Statistical characterization and stochastic modeling of pore networks in relation to fluid flow. *Mathematical Geosciences*, 29: 801–822.

Hinrichsen, E.L., Feder, J., Jøssang, T., 1990. Random packing of disks in two dimensions. *Physical Review A,* 41(8): 4199–4209.

Isakov, E., Ogilvie, S.R., Taylor, C.W. and Glover, P.W.J., 2001. Fluid flow through rough fractures in rocks I: High resolution aperture determinations. *Earth and Planetary Science Letters*, 191(3-4), pp. 267-282.

Jin, G., Patzek, T.W., Silin, D.B., 2003. Physics-based reconstruction of sedimentary rocks. *SPE*, 83587.

Jin, X.C., Ong, S.H., Jayasooriah, 1995. A practical method for estimating fractal dimension. *Pattern Recognition Letters*, 16: 457–464.

Kamann, P.J., Ritzi, R.W., Dominic, D.F., et al., 2007. Porosity and permeability in sediment mixtures. *Ground Water,* 45(4): 429–438.

Karimpouli, S., Tahmasebi, P., 2019. 3D Multifractal Analysis of Porous Media Using 3D Digital Images: Considerations for heterogeneity evaluation. *Geophysical Prospecting*, 67:1082-1093

Katz, A. J., Thompson, A. H., 1985. Fractal sandstone pores: Implications for conductivity and pore formation. *Physical Review Letter,* 54: 10325–10328.

Krohn, C.E., 1988a. Sandstone fractal and Euclidean pore volume distributions. *Journal of Geophysical Research,* 93(B4): 3286-3296.

Krohn, C.E., 1988b. Fractal measurements of sandstones, shales, and carbonates. *Journal of Geophysical Research,* 93(B4): 3297-3305.

Latief, F.D.E., Biswal, B., Fauzi, U., et al., 2010. Continuum reconstruction of the pore scale microstructure for Fontainebleau sandstone. *Physica A*, 389: 1607–1618.

Li, J., Du, Q., Sun, C., 2009. An improved box-counting method for image fractal dimension estimation. *Pattern Recognition*, 42: 2460–2469.

Li, X., Luo, M., Liu, J., 2019. Fractal characteristics based on different statistical objects of process-based digital rock models. *Journal of Petroleum Science and Engineering*, 179: 19–30

Luo, M., Pan, H., 2015. A numerical study on the relation between the electrical spectra of a mixture and the electrical properties of the components of the mixture. *Journal of Applied Geophysics,* 112: 33–41.

Mandelbrot, B., 1975. Les objets fractals: forme, hasard et dimension. Flammarion (Eds): Paris, 208 pp.

Mandelbrot, B. 1982. The Fractal Geometry of Nature. Freeman, San Francisco, CA.

Muller, J., 1996. Characterization of pore space in chalk by multifractal analysis. *Journal of Hydrology*, 187: 215–222.

Nilsen, L.S., Øren, P.E., Bakke, S., 1996. Prediction of relative permeability and capillary pressure

from a pore model. *SPE,* 35531.

Ogilvie, S.R., Orribo, J.M., Glover, P.W.J., 2001. The influence of deformation bands upon fluid flow using profile permeametry and positron emission tomography. *Geophysical Research Letter,* 28(1): 61–64.

Ogilvie, S.R., Isakov, E., Taylor, C.W. and Glover, P.W.J., 2003. Characterization of rough-walled fractures in crystalline rocks. Geol. Soc. Spec. Publ., 214, pp. 125-141.

Ogilvie, S.R., Isakov, E., Glover, P.W.J., 2006. Fluid flow through rough fractures in rocks. II: A new matching model for rough rock fractures. *Earth and Planetary Science Letters,* 241(3-4): 454–465.

Okabe, H., Blunt, M.J., 2005. Pore space reconstruction using multiple-point statistics. *Journal of Petroleum Science and Engineering,* 46: 121–137.

Øren, P.E., Bakke, S., 2002. Process based reconstruction of sandstones and prediction of transport properties. *Transport in Porous Media,* 46: 311–343.

Pape, H., Clauser, C., Iffland, J., 1999. Permeability prediction based on fractal pore-space geometry. *Geophysics,* 64(5): 1447–1460.

Peitgen, H.O., Jurgens, H., Saupe, D., 1992. Chaos and Fractals New Frontiers of Science. Springer, New York.

Peleg, S., Naor, J., Hartley, R., Avnir, D., 1984. Multiple resolution texture analysis and classification. *IEEE Transactions on Pattern Analysis and Machine Intelligence*, 6 (4): 518–523.

Pilotti, M., 2000. Reconstruction of clastic porous media. *Transport in Porous Media,* 41(3): 359–364.

Pruess, S., 2007. In: Barton, C.C., Pointe, P.R. (Eds.), Some remarks on the numerical estimation of fractal dimension: Fractals in the Earth Sciences, 3. Plenum Press, New-York, pp. 65–75.

Renard, F., Dysthe, D., 2003. Pressure solution. In: Encyclopedia of Sediments and Sedimentary Rocks (Ed. Middleton, G.V.). Kluwer Academic Publishers, Dordrecht; 542–543.

Revil, A., Glover, P., 1998. Nature of Surface Electrical Conductivity in Natural Sands, Sandstones, and Clays. *Geophysical Research Letters,* 25: 691–695.

Roth, S., Biswal, B., Afshar, G., et al., 2011. Continuum-based rock model of a reservoir dolostone with four orders of magnitude in pore sizes. *AAPG Bulletin,* 95: 925–940.

Russell, D.A., Hanson, J., Ott, E., 1980. Dimension of strange attractors. *Physical Review Letters,* 45(14): 1175–1178.

Sarkar, N., Chaudhuri, B.B., 1992. An efficient approach to estimate fractal dimension of textural images. *Pattern Recognition,* 25: 1035–1041.

Schroeder, M., 1991. Fractals, Chaos, Power Laws. Freeman, New York.

Schlueter, E.M., Zimmermana, R.W., Witherspoon, P.A., et al., 1997. The fractal dimension of pores in sedimentary rocks and its influence on permeability. *Engineering Geology,* 48(3–4): 199–215.

Shelberg, M., Lam, N., Moellering, H., 1983. Measuring the fractal dimension of surfaces. Proceedings of the Sixth International Symposium on Computer-Assisted Cartography Auto-Carto 6, 319–328.

Suman, R., Knight, R., 1997. Effects of pore structure and wettability on the electrical resistivity of partially saturated rocks — a network study. *Geophysics,* 62: 1151–62.

Tahmasebi, P., Sahimi, M., 2012 Reconstruction of three-dimensional porous media using a single thin section. *Physical Review E*, 85, 066709

Tang, H.P., Wang, J.Z., Zhu, J.L., et al., 2012. Fractal dimension of pore-structure of porous metal materials made by stainless steel powder. *Powder Technology*, 217: 383–387

Tarafdar, S., Roy, S., 1998. A growth model for porous sedimentary rocks. *Physica B,* 254: 28–36.

Tarboton, D.G., Bras, R.L. & Rodriguez-Iturbe, I., 1988. The fractal nature of river networks. *Water Resources Research,* 24(8): 1317–1322.

Turner, M., Blackledge, J., Andrews, P., 1998. Fractal geometry in digital imaging. Academic Press, London.

Walker, E., Glover P.W.J., Ruel, J., 2014. A transient method for measuring the DC streaming potential coefficient of porous and fractured rocks. *Journal of Geophysical Research,* 119: 957–970.

Wang, H., Liu, Y., Song, Y., et al., 2012. Fractal analysis and its impact factors on pore structure of artificial cores based on the images obtained using magnetic resonance imaging. *Journal of Applied Geophysics*, 86: 70–81.

Wang, J.G., Hu, B.W., Wu, D., et al., 2019. A Multiscale Fractal Transport Model with Multilayer Sorption and Effective Porosity Effects. Transport in Porous Media. 129(1): 25-51

Wong, P., Howard, J., Lin, J., 1986. Surface roughening and the fractal nature of rocks. *Physical Review Letters,* 57: 637–640.

Wu, Y., Tahmasebi, P., Lin, C., Jawad Munawar, M., Cnudde, V., 2019. Effects of Micropores on Geometric, Topological and Transport Properties of Pore Systems for Low-Permeability Porous Media. *Journal of Hydrology*, 575: 327-342

Wu, Y., Tahmasebi, P., Yu, H., Lin, C., Dong, C., 2020a. Process-based and dynamic 2D modeling of shale samples: Considering the geology and pore-system evolution. *International Journal of Coal Geology*, 218: 103368

Wu, Y., Tahmasebi, P., Yu, H., Lin, C., Wu, H., Dong, C., 2020b. Pore-scale 3D Dynamic Modeling and Characterization of Shale Samples: Considering the Effects of Thermal Maturation. *Journal of Geophysical Research: Solid Earth*, 125(1), https://doi.org/10.1029/2019JB018309

Xie, H., 1993. Fractals in rock mechanics, Balkema Publisher, Netherlands.

Xu, S., Weng, Y., 2006. A new approach to estimate fractal dimensions of corrosion images. *Pattern Recognition Letters,* 27: 1942–1947.

Yang, F., Ning, Z., Liu, H., 2014. Fractal characteristics of shales from a shale gas reservoir in the Sichuan Basin, China. *Fuel*, 115: 378-384

Yeong, C.L.Y., Torquato, S., 1998. Reconstructing random media. *Physical Review E,* 57 (250): 495–506.

Yu, B., Cheng, P., 2001. A fractal permeability model for bi-dispersed porous media. *International Journal of Heat and Mass Transfer,* 45: 2983–2993.

Yu, P., Duan, Y. H., Chen, E., et al., 2018. Microstructure-based fractal models for heat and mass transport properties of cement paste. *International Journal of Heat and Mass Transfer*, 126: 432-447

Zhang, F., Ward, A.L., Keller, J.M., 2009. Determining the porosity and saturated hydraulic conductivity of binary mixtures. US DoE Report, PNNL-18801.

Zhao J., Sun J., Liu X., et al., 2013. Numerical simulation of the electrical properties of fractured rock based on digital rock technology. *Journal of Geophysics and Engineering,* 10(5):1-6.

Zhu, W., Yu, W., Chen, Y., 2012. Digital core modeling from irregular grains. *Journal of Applied Geophysics,* 85(1): 37–42.

Table 1. Porosity, specific surface area and fractal dimension (D) of the 3D models composed of round grains with different grain-size varieties (GSV). (R: grain radius; S_{Sp}: specific surface area; D_i: fractal dimension of the interface between the pore and grains in a 3D model; D_v: fractal dimension of the pore volume in a 3D model; D_b: interface fractal dimension derived from a 2D slice; D_a: pore area fractal dimension derived from a 2D slice).

Model No.	GSV (unit)	Porosity (fractional)	S_{Sp} ($\mu m^2/\mu m^3$)	D_i (-)	D_v (-)	D_b (-)	D_a (-)
V1	$R = 26$	0.378	0.274	2.747	2.853	1.641	1.816
V2	$R = 26,23$	0.377	0.278	2.755	2.858	1.666	1.834
V3	$R = 26,23,20$	0.367	0.302	2.767	2.859	1.666	1.827
V4	$R = 26,23,20,17$	0.360	0.326	2.779	2.861	1.672	1.827
V5	$R = 26,23,20,17,14$	0.348	0.354	2.788	2.861	1.700	1.819
V6	$R = 26,23,20,17,14,11$	0.335	0.383	2.796	2.859	1.704	1.825
V7	$R = 26,23,20,17,14,11,8$	0.331	0.394	2.799	2.858	1.708	1.810

Table 2. Porosity, specific surface area and fractal dimension (D) of the 3D models composed of round grains with different compaction coefficients (C_p). (Por: Porosity; S_{Sp}: specific surface area; D_i: fractal dimension of the interface between the pore and grains in a 3D model; D_v: fractal dimension of the pore volume in a 3D model; D_b: interface fractal dimension derived from a 2D slice; D_a: pore area fractal dimension derived from a 2D slice).

| C_p	Porosity	S_{Sp}	D_i	D_v	D_b	D_a
(-)	(fractional)	($\mu m^2/\mu m^3$)	(-)	(-)	(-)	(-)
0.000	0.343	0.390	2.806	2.867	1.714	1.830
0.030	0.335	0.407	2.809	2.866	1.719	1.825
0.060	0.275	0.482	2.800	2.842	1.707	1.795
0.090	0.215	0.573	2.780	2.811	1.679	1.748
0.120	0.159	0.685	2.750	2.771	1.640	1.691
0.150	0.109	0.813	2.704	2.717	1.605	1.643
0.180	0.069	0.963	2.636	2.644	1.505	1.530
0.210	0.038	1.164	2.539	2.543	1.368	1.387
0.240	0.018	1.436	2.403	2.405	1.200	1.213

Table 3. Porosity, specific surface area and fractal dimension of 3D models with different cementation thickness (T_c). (S_{Sp}: specific surface area; D_i: fractal dimension of the interface between the pore and grains in a 3D model; D_v: fractal dimension of the pore volume in a 3D model; D_b: interface fractal dimension derived from a 2D slice; D_a: pore area fractal dimension derived from a 2D slice).

T_c (unit)	Porosity (fractional)	S_{Sp} ($\mu m^2/\mu m^3$)	D_i (-)	D_v (-)	D_b (-)	D_a (-)
0	0.360	0.326	2.779	2.861	1.672	1.827
1	0.322	0.352	2.770	2.844	1.675	1.808
2	0.257	0.406	2.747	2.806	1.656	1.765
3	0.202	0.462	2.717	2.765	1.624	1.713
4	0.142	0.539	2.666	2.702	1.566	1.633
5	0.100	0.605	2.605	2.634	1.497	1.550
6	0.063	0.694	2.517	2.538	1.388	1.428
7	0.043	0.767	2.440	2.457	1.294	1.331
8	0.029	0.849	2.359	2.371	1.192	1.223

Table 4. Measurement and computation result of the sedimentary rock samples (micro-CT image and permeability data released by Dong and Blunt (2009)). (S_{Sp}: specific surface area; D_i: fractal dimension of the interface between the pore and grains in a 3D model; D_v: fractal dimension of the pore volume in a 3D model; D_b: interface fractal dimension derived from a 2D slice; D_a: pore area fractal dimension derived from a 2D slice; σ: succolarity).

Sample code	Permeability (mD)	S_{Sp} ($\mu m^2/\mu m^3$)	Porosity (-)	D_i (-)	D_v (-)	σ (-)
S1	1678	0.61879	0.142	2.623	2.656047	0.152228
S2	3898	0.538668	0.245	2.747	2.789885	0.24284
S3	224	1.061754	0.168	2.823	2.82907	0.168731
S4	259	1.055709	0.171	2.840	2.845779	0.170505
S5	4651	0.309189	0.220	2.535	2.657774	0.228538
S6	10974	0.315747	0.230	2.547	2.669289	0.317245
S7	6966	0.407074	0.261	2.676	2.754173	0.266872
S8	13169	0.419867	0.338	2.766	2.837893	0.334378
C1	1102	0.500079	0.211	2.662	2.724738	0.227373
C2	72	0.667869	0.146	2.633	2.667248	0.175625
Berea sandstone	1286	0.640334	0.197	2.735	2.765244	0.1991
A1	7220	0.507309	0.422	2.880	2.929091	0.320865
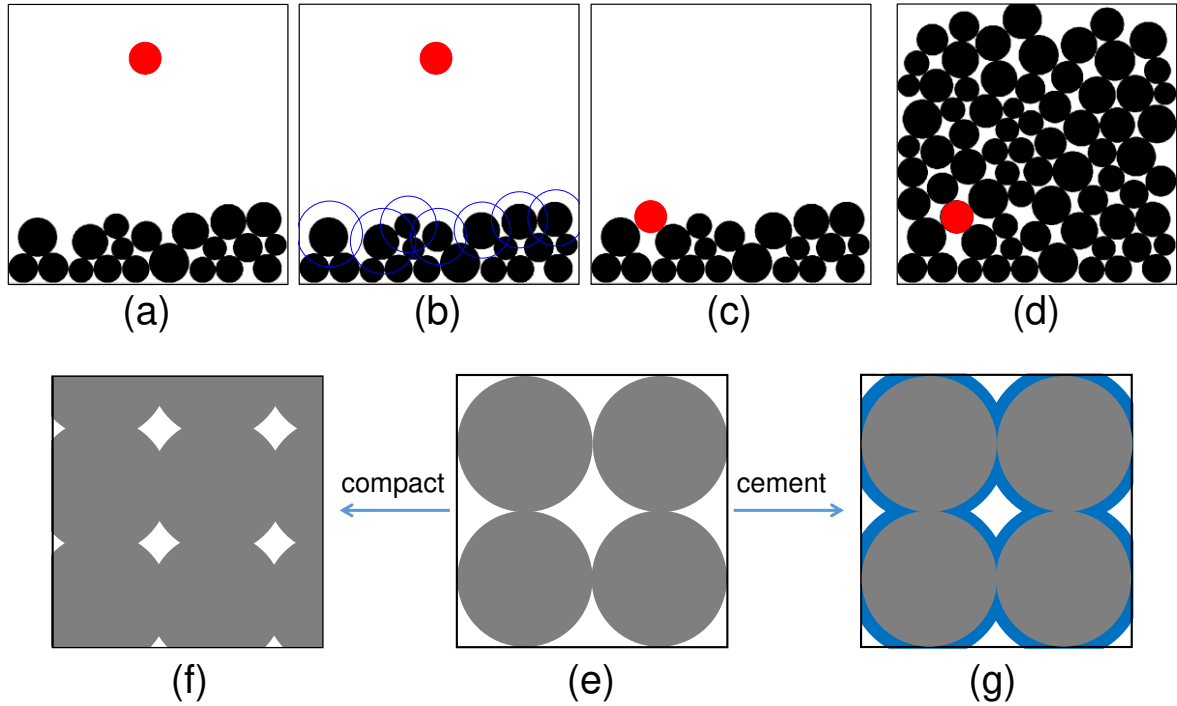
Fig. 1. Schematic diagram of the process-based digital rock modeling, including sedimentation, compaction and cementation effects. (a) One new (red) grain is generated and falling. The grain size is generated stochastically from a predetermined final grain size distribution. (b) All the deposited grains are expanded according to the radius of the new grain and form a deposit surface where the center of the new grain can be placed at. (c) The new grain finds the lowest point on the deposit surface and gets to the most stable position. (d) The final image of the digital rock model. (e) Initial model without compaction (compaction coefficient $C_p = 0$) and cementation (cementation thickness $T_c = 0$). (f) The model with compaction effect ($C_p = 0.15$). (g) The model with cementation effect ($T_c = 4$ unit).
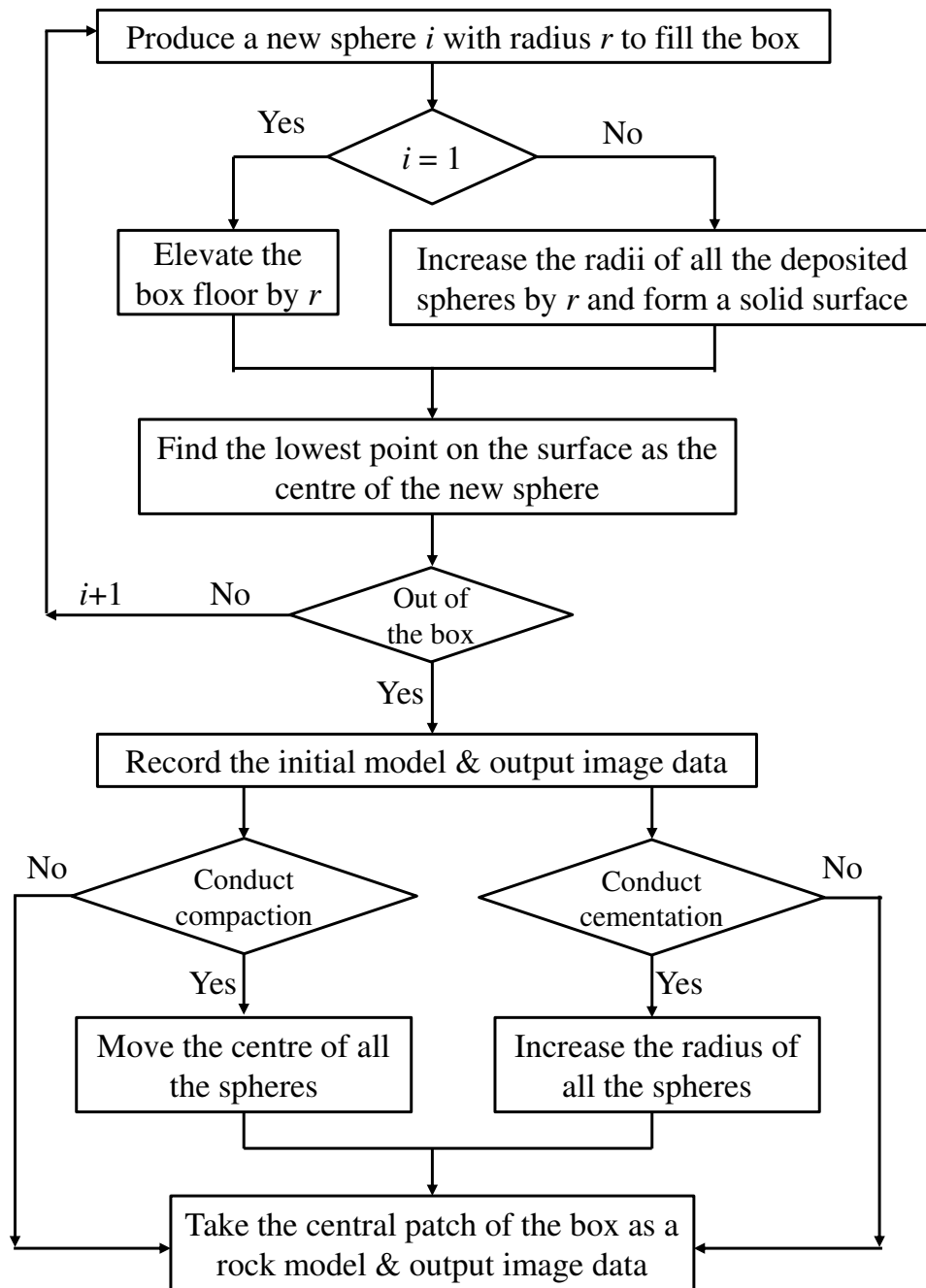
Fig. 2. Flowchart of the process-driven digital rock model construction.
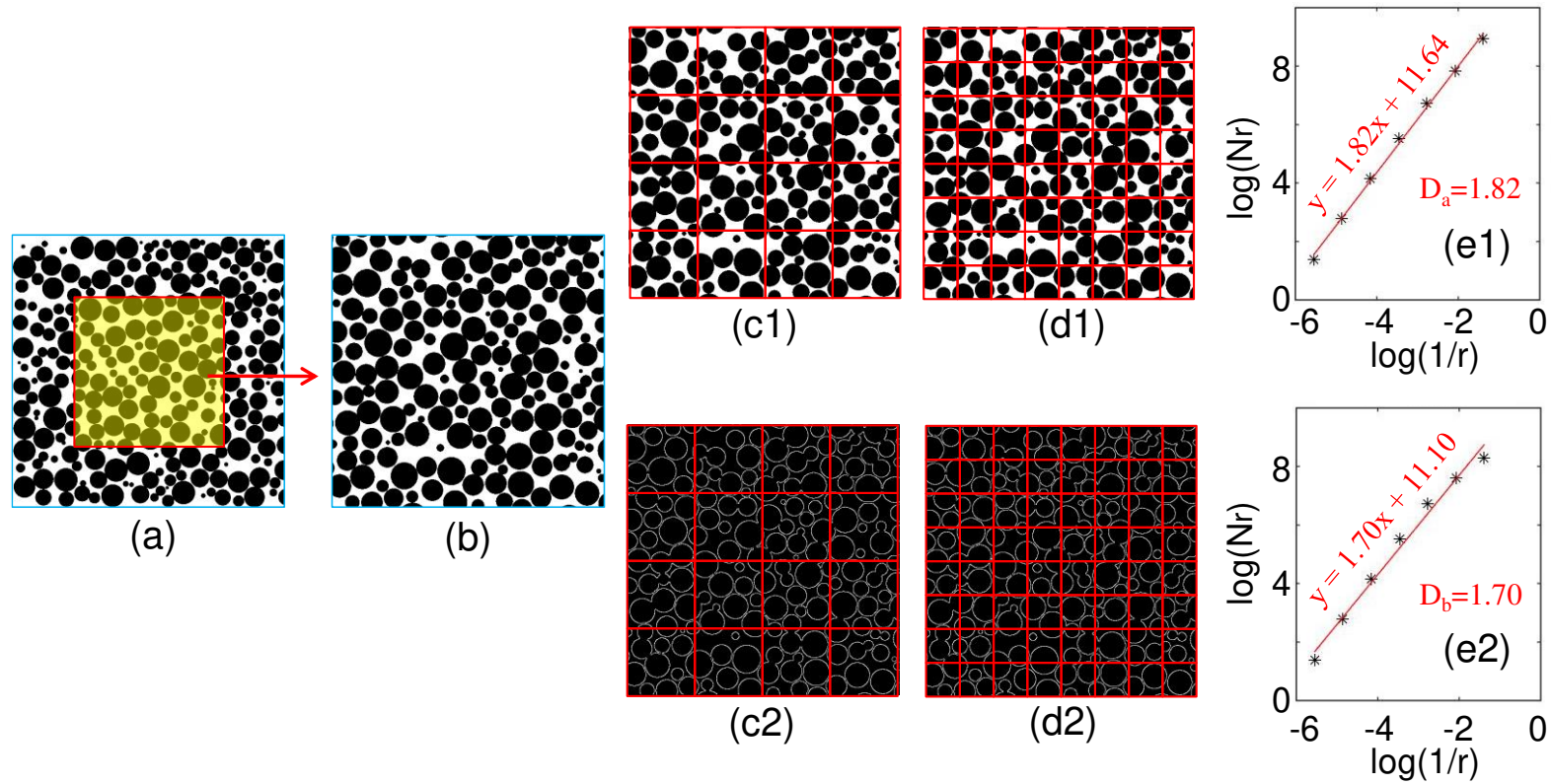
Fig. 3. Schematic diagram of the fractal dimension calculation of a 2D image by the box-counting method (The image data come from the model V5 of Table 1) . (a) Image of the entire 2D digital rock model (white for pores; black for grains). (b) 512×512 sub-image of the entire model. (c1) Sub-image divided by a $n \times n$ grid with a side-length $r_n = 512/n$, for which the number N_{rn} of boxes containing white (pores) is counted. (d1) Sub-image divided by a denser $m \times m$ grid, used to obtain a new box count number N_{rm}. (e1) A linear fit to the plot of $\log(N_r)$ versus $\log(1/r)$, the slope of which is the fractal dimension (D_a) of pore areas. (c2) The sub-image digitally filtered to show in white only those pixels at the interface between pores and grains. The sub-image is divided by a $n \times n$ grid with a side-length $r_n = 512/n$, for which the number N_{rn} of boxes containing white (borders) is counted. (d2) Filtered sub-image divided by a denser $m \times m$ grid, used to obtain a new box count number N_{rm}. (e2) A linear fit to the plot of $\log(N_r)$ versus $\log(1/r)$, the slope of which is the fractal dimension (D_b) of borders between pores and grains.
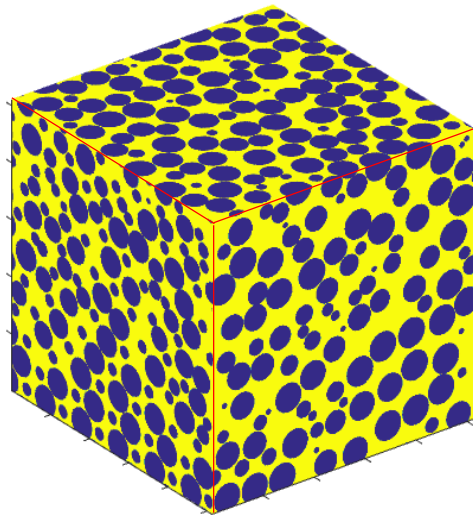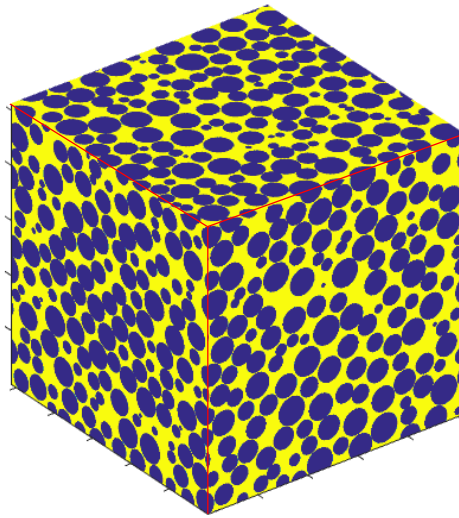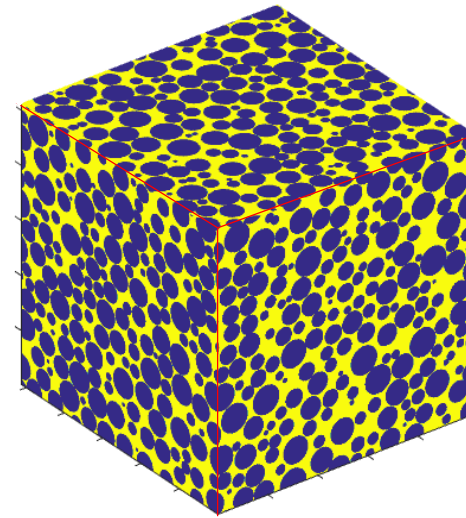
(a) V1   **(b) V4**   **(c) V7**

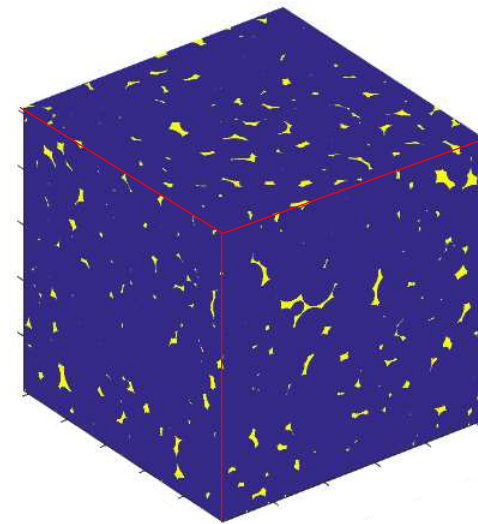**Fig. 4.** 3D digital rock models with different grain size variety (Table 1 shows the grain size variety parameters of each model).
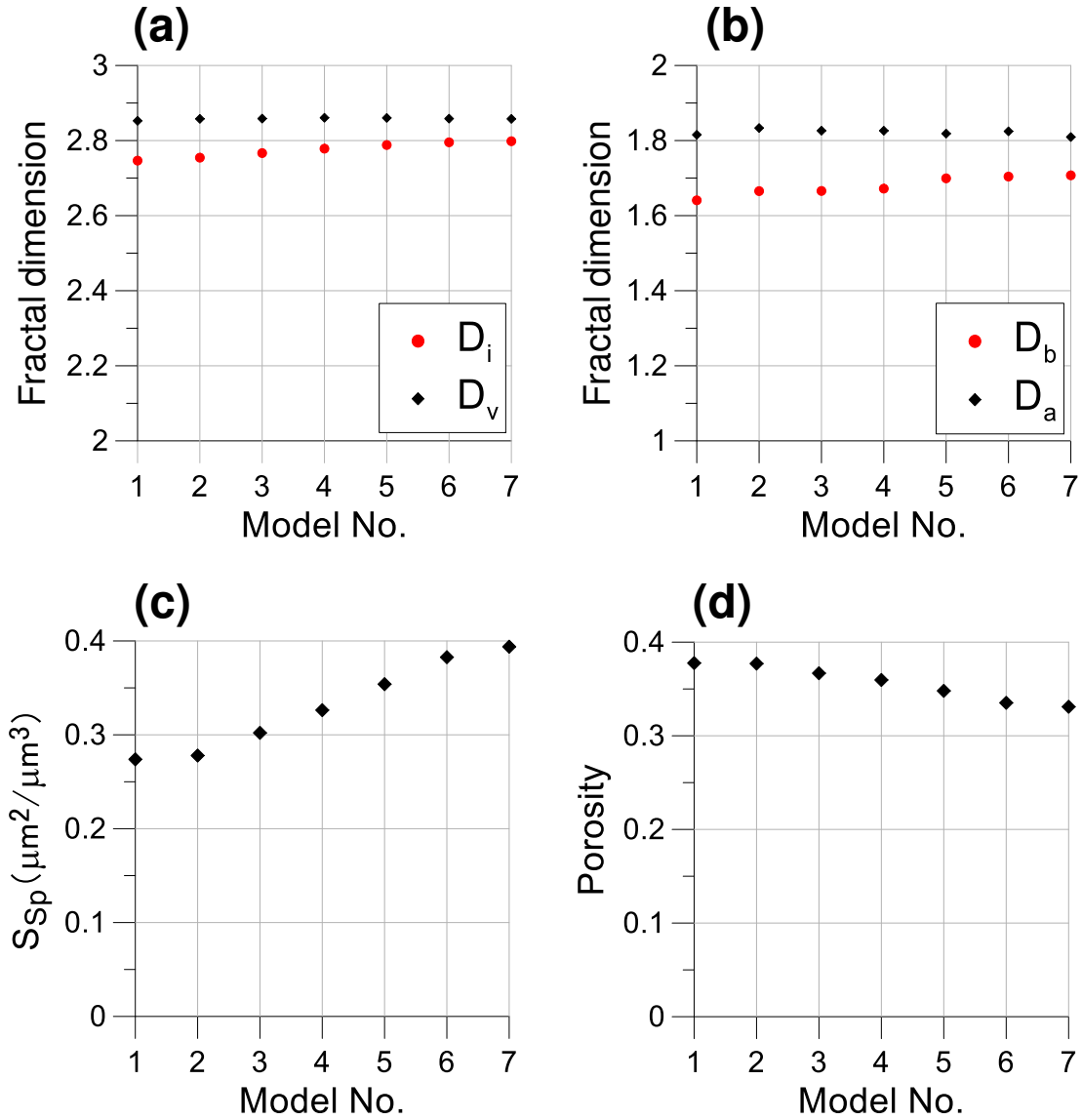
Fig. 5. Variation of porosity, specific surface area and fractal dimension with the grain size variety (S_{Sp}: specific surface area; D_i: fractal dimension of the interface between the pore and grains in a 3D model; D_v: fractal dimension of the pore volume in a 3D model; D_b: interface fractal dimension derived from a 2D slice; D_a: pore area fractal dimension derived from a 2D slice). S_{Sp} is defined as the ratio of the total surface area of pore space to the total volume of pore space.

(a) C_p=0 **(b) C_p=0.12** **(c) C_p=0.24**
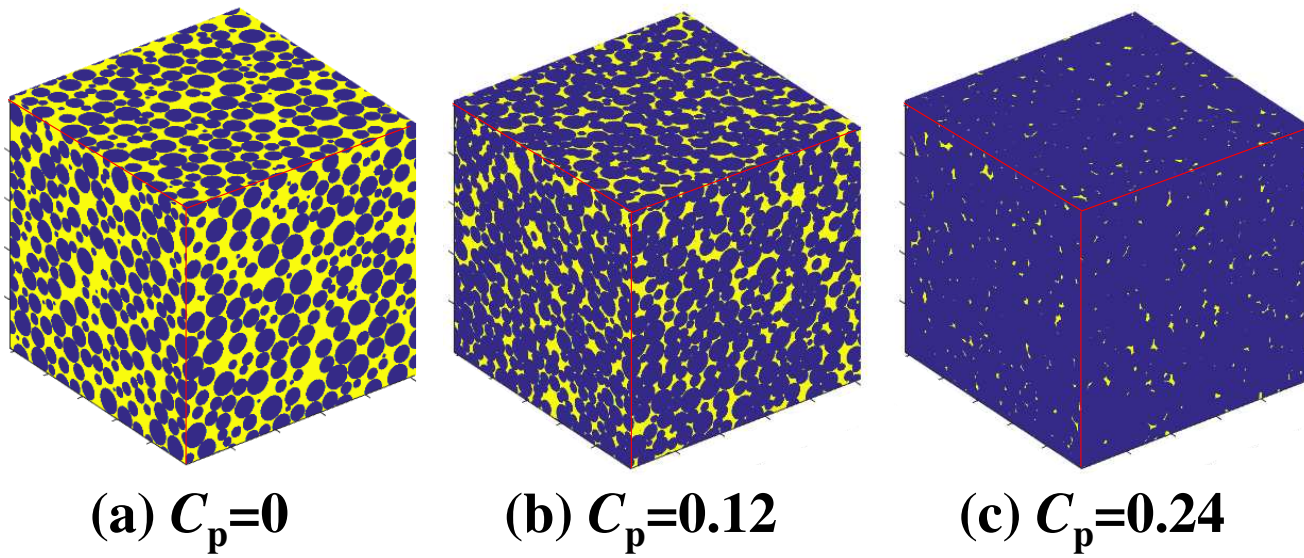
Fig. 6.   3D digital rock models with different compaction coefficient (C_p).
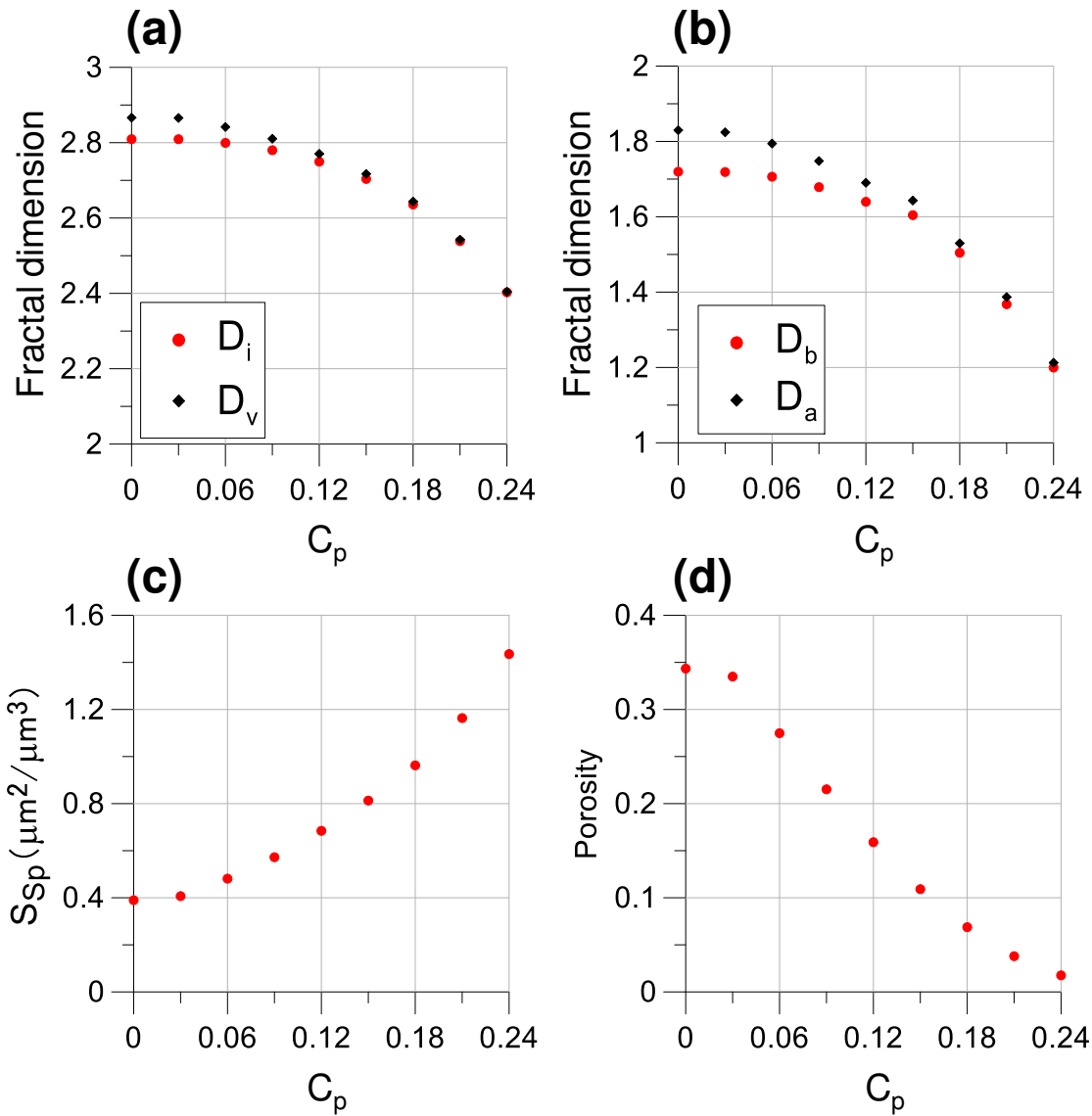
Fig. 7.　Variation of porosity, specific surface area and fractal dimension with the compaction coefficient (C_p) (S_{Sp}: specific surface area; D_i: fractal dimension of the interface between the pore and grains in a 3D model; D_v: fractal dimension of the pore volume in a 3D model; D_b: interface fractal dimension derived from a 2D slice; D_a: pore area fractal dimension derived from a 2D slice). S_{Sp} is defined as the ratio of the total surface area of pore space to the total volume of pore space.

31
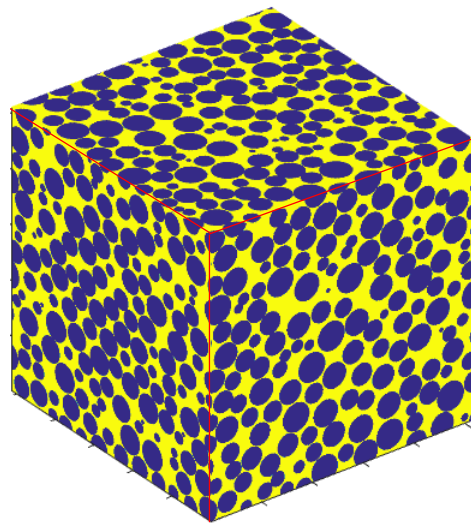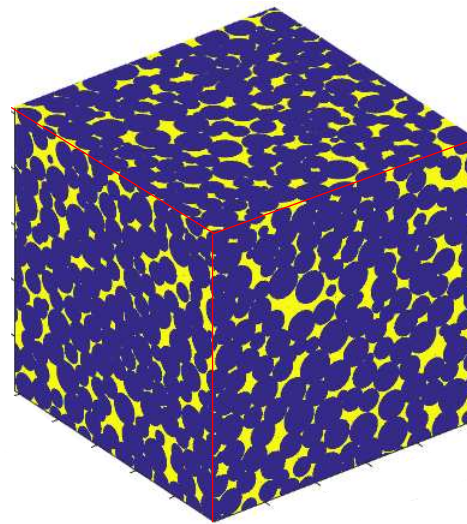
(a) $T_c = 0$ **(b)** $T_c = 4$ **(c)** $T_c = 8$

Fig. 8. 3D digital rock models with different cementation thickness (T_c).
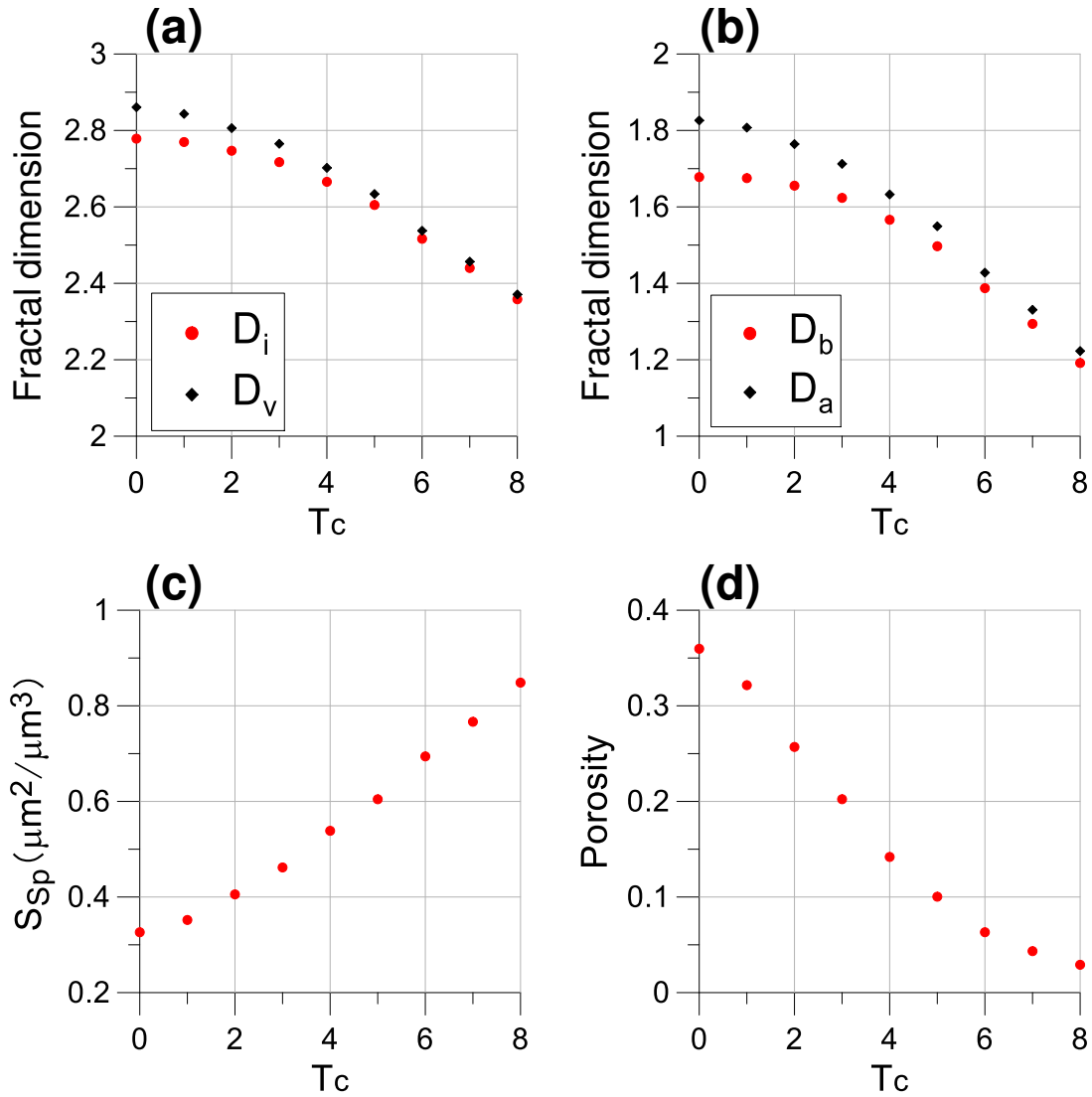
Fig. 9. Variation of porosity, specific surface area and fractal dimension with the cementation thickness (T_c) (S_{Sp}: specific surface area; D_i: fractal dimension of the interface between the pore and grains in a 3D model; D_v: fractal dimension of the pore volume in a 3D model; D_b: interface fractal dimension derived from a 2D slice; D_a: pore area fractal dimension derived from a 2D slice). S_{Sp} is defined as the ratio of the total surface area of pore space to the total volume of pore space.
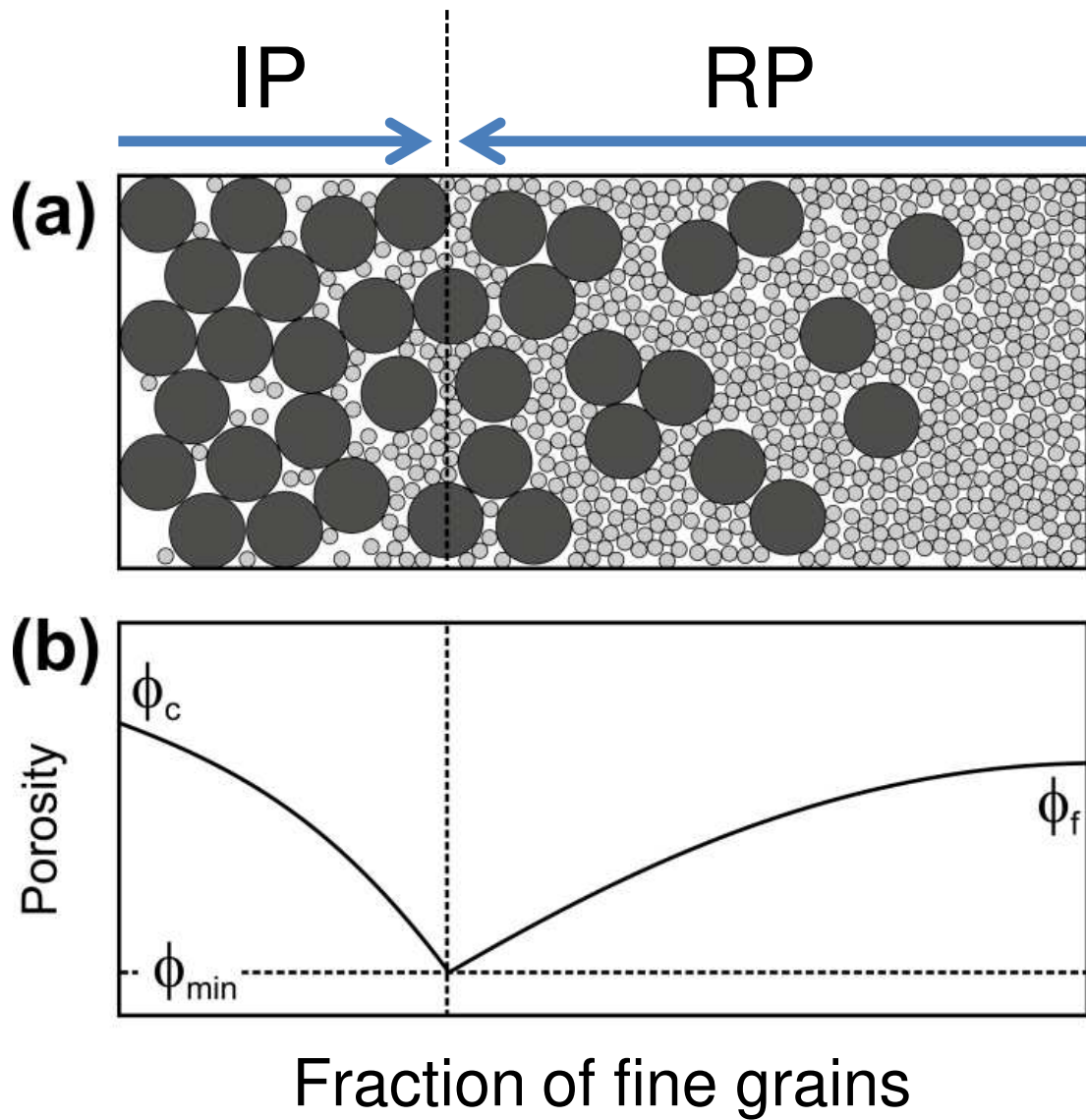
Fig. 10. (a) Schematic diagram of a 2D binary mixture of sphere grains. IP: Interstitiation Process; RP: Replacement Process. (b) Porosity versus fraction of fine grains. ϕ_c: porosity of coarse grains; ϕ_f: porosity of fine grains; ϕ_{min}: the minimum porosity (after Glover and Luo, 2020).
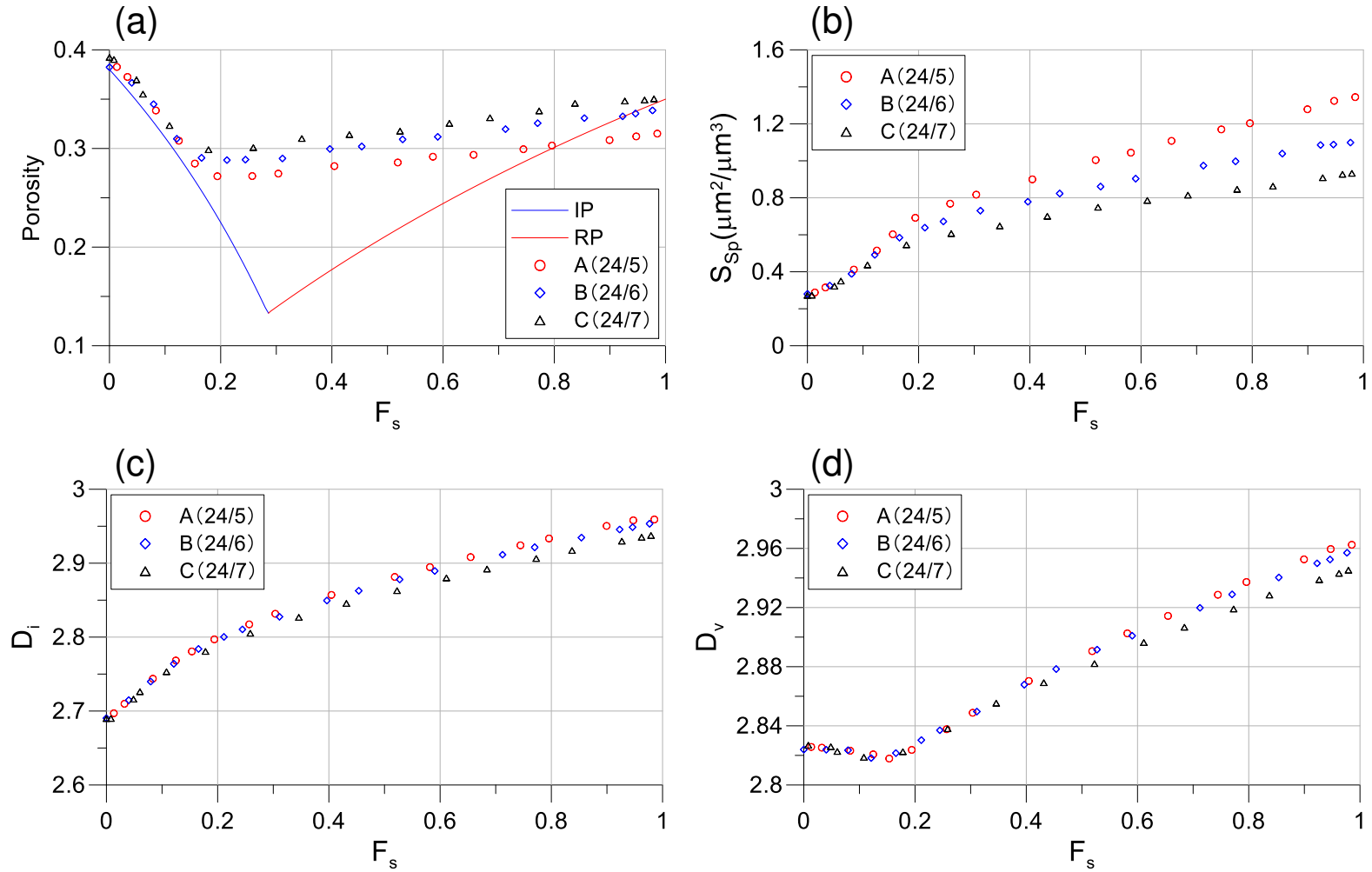
Fig. 11. Results from process-driven DRM and theory for binary grain mixtures. (a) Porosity, (b) specific surface area, (c) D_i, and (d) D_v, each as a function of the fraction of fine grains. (Solid line is from the theoretical model; IP: Interstitiation Process; RP: Replacement Process; circles - Binary Model A ($r_c/r_f = 24/5$); diamonds - Binary Model B ($r_c/r_f = 24/6$); triangles - Binary Model C ($r_c/r_f = 24/7$); r_c: radius of the coarse grains; r_f: radius of the fine grains).
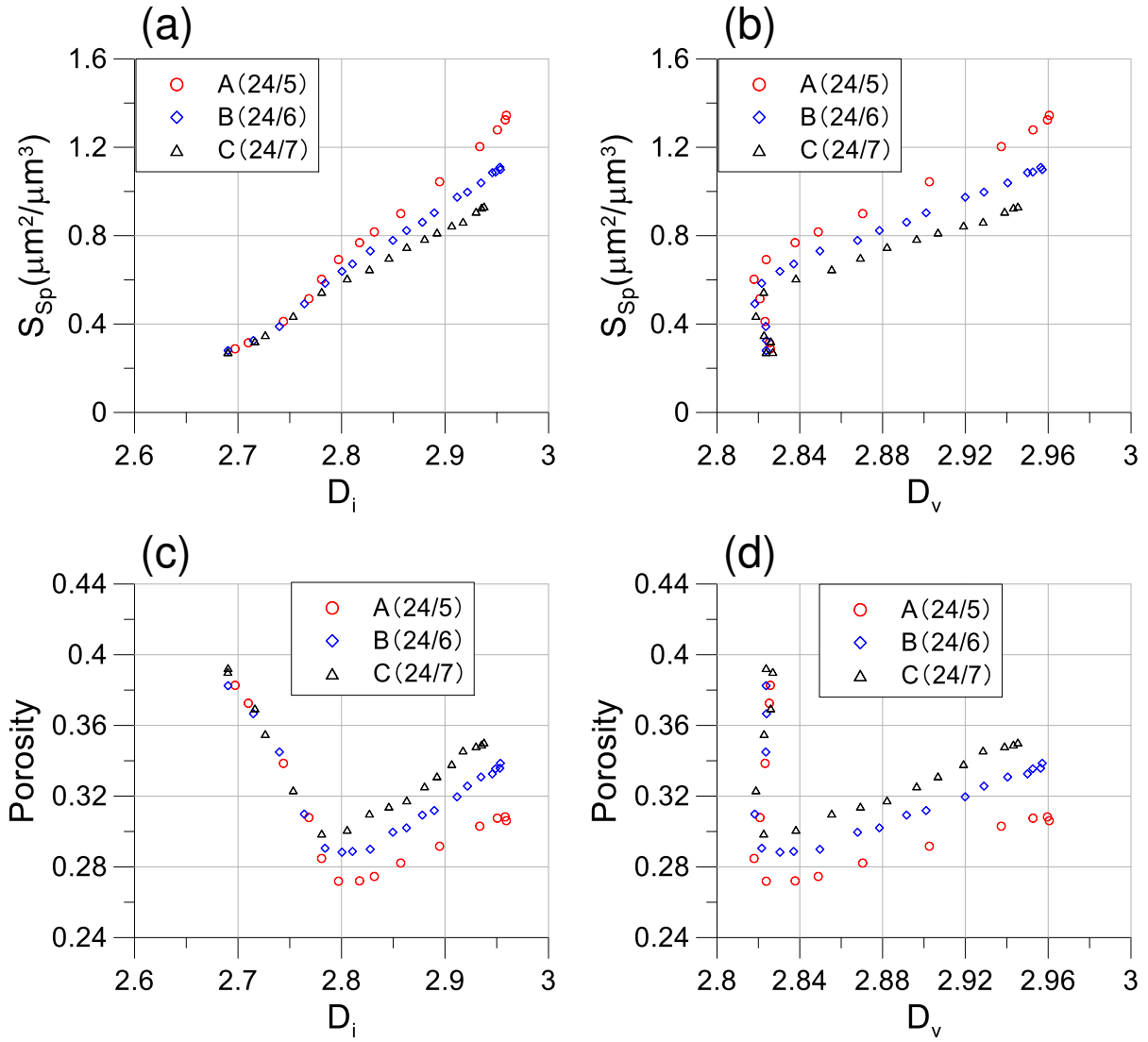
Fig. 12. Cross-plots of fractal dimensions against specific surface area (panels a and b) and porosity (panels c and d). S_{Sp} is defined as the ratio of the total surface area of pore space to the total volume of pore space.
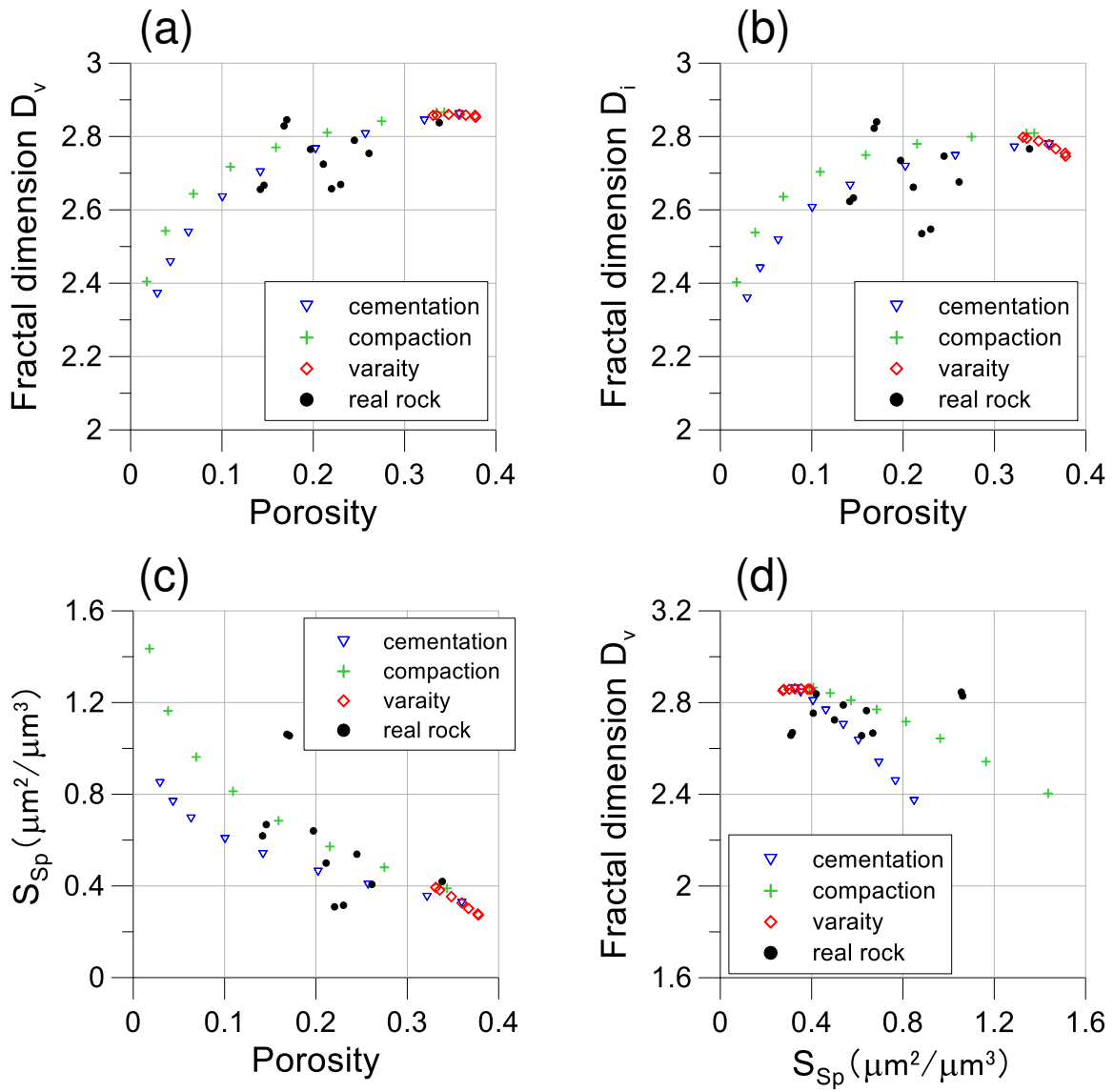
Fig. 13. Cross-plots of porosity against fractal dimension and specific surface area (S_{Sp}) and S_{Sp} against fractal dimension.
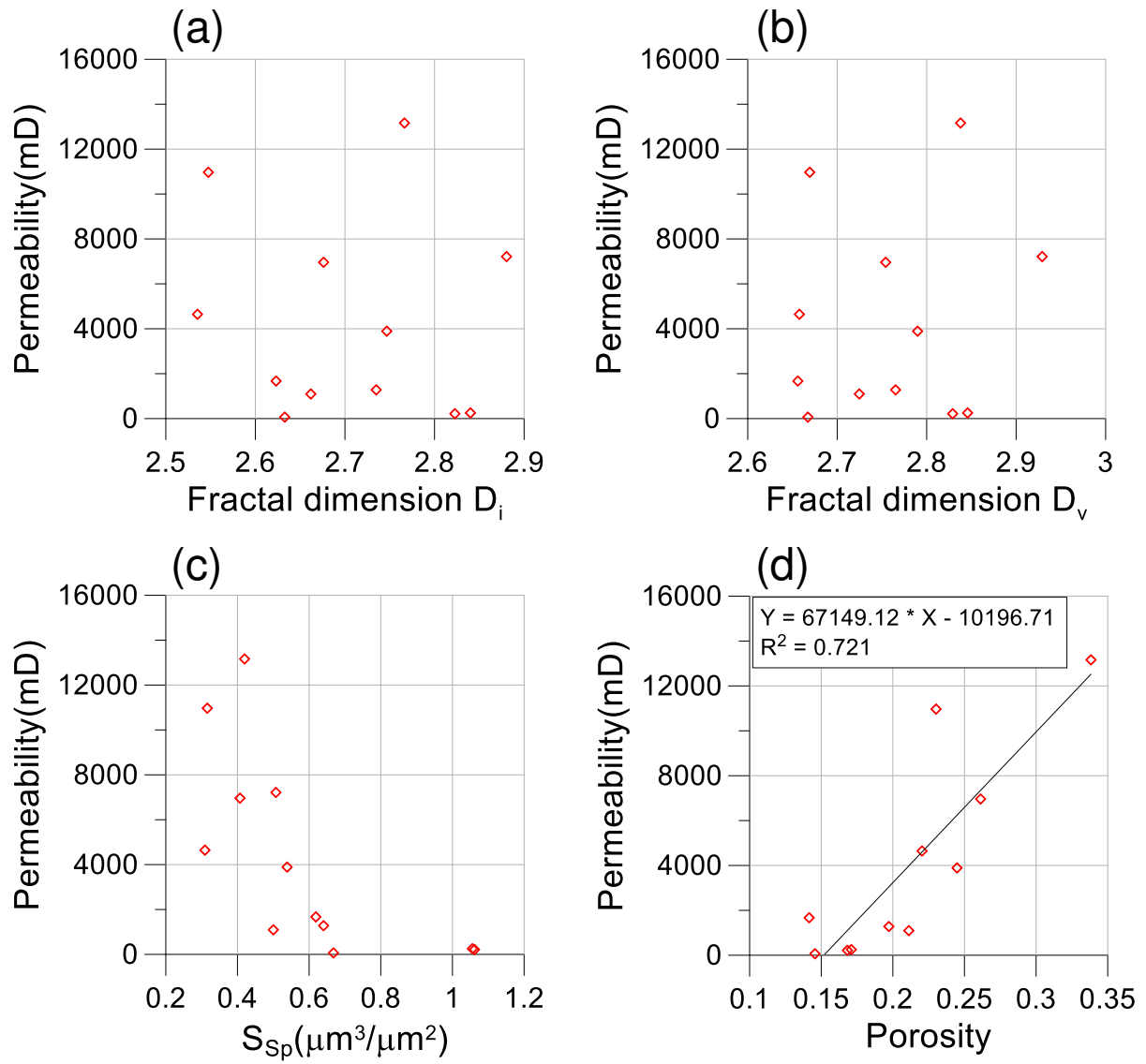
Fig. 14. Cross-plots of permeability against the main petrophysical parameters. (a) Permeability as a function of D_i. (b) Permeability as a function of D_v. (c) Permeability as a function of specific surface area. (d) Permeability as a function of porosity.
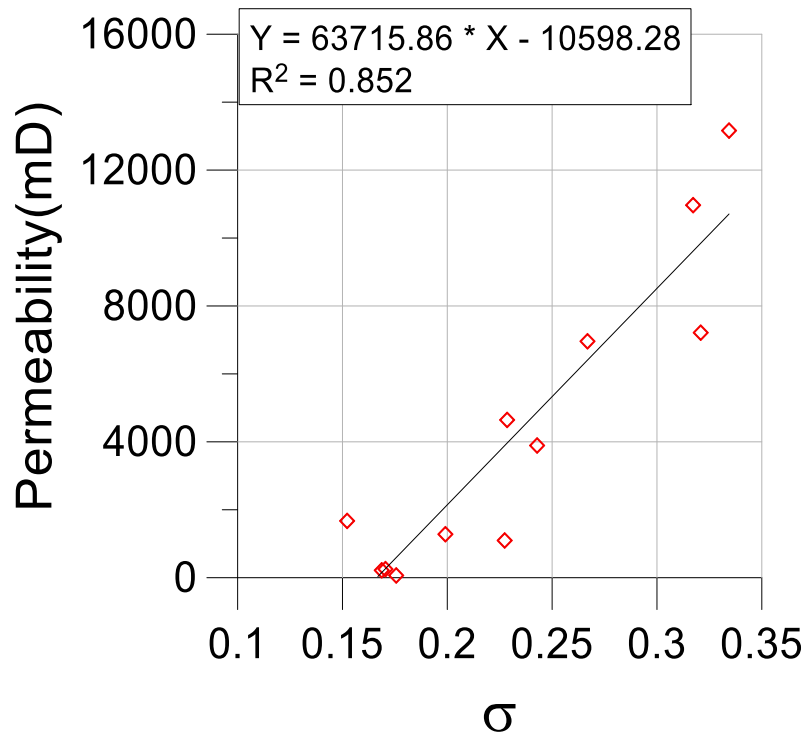
Fig. 15. Permeability as a function of succolarity (σ).
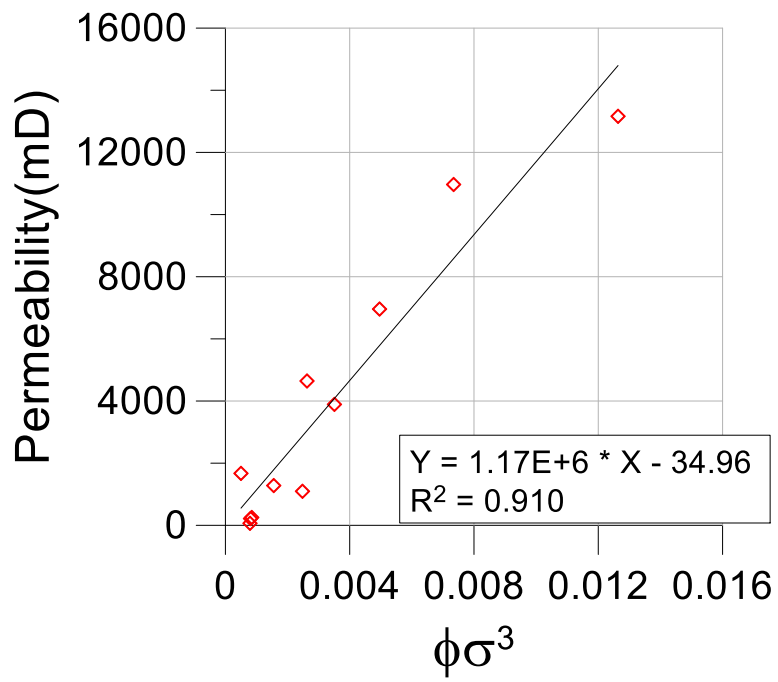
Fig. 16. Permeability as a function of the product $\phi\sigma^3$.